Coherent Fourier scatterometry combined with synthetic optical holography for nanoparticle detection

H. Yin

Delft University of Technology
Faculty of Applied Sciences
Department of Imaging Physics

Master Thesis Project

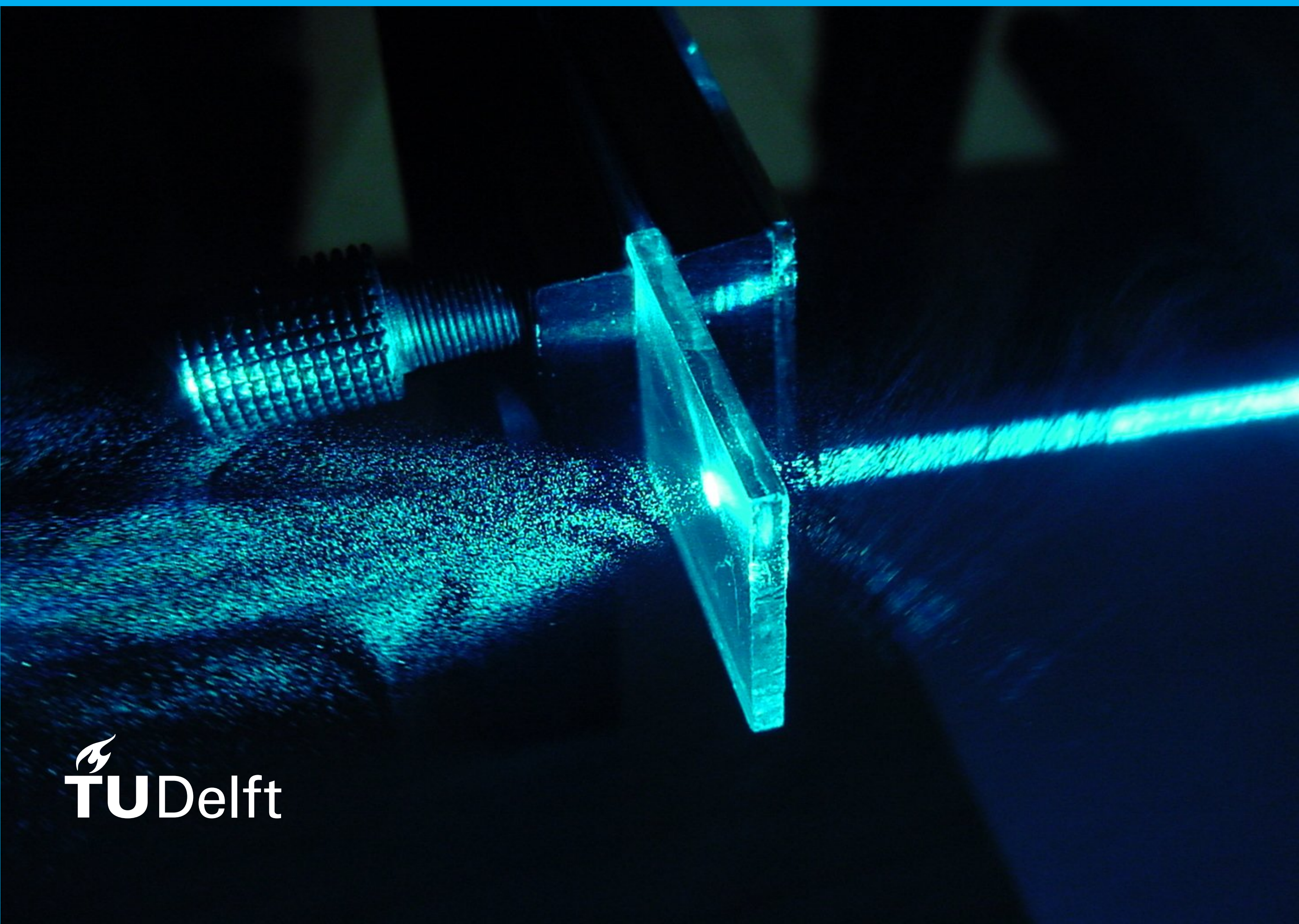

Coherent Fourier scatterometry combined with synthetic optical holography for nanoparticle detection

by

H. Yin

in partial fulfillment of the requirements for the degree of
Master of Science in Applied Physics
at the Delft University of Technology,

Student number:	4687337	
Project duration:	August 30, 2021 – April 1, 2022	
Thesis committee:	Dr. S.F. Pereira	TU Delft, supervisor
	Dr. O. El Gawhary	TU Delft, examiner
	Dr. J. Kalkman	TU Delft, examiner

TU Delft Delft University of Technology ImPhys Optics Research Group

Abstract

As demand for chips increases and critical dimension keeps shrinking, the inspection of wafer becomes one of the critical challenges in the high volume production of chips. Coherent Fourier scatterometry (CFS) is a scanning bright field technique that is capable to detect nanoparticles on Si surfaces. The optical readout of CFS consists of a two pixel split detector that gives a voltage signal based on the intensity difference between the two halves. While an area of the wafer is raster scanned, the flat surface with no particles gives a zero voltage and on the particle an asymmetrical (non-zero) signal will be detected.

In this thesis, we demonstrate the use of synthetic optical holography (SOH) as a new method to improve the sensitivity of CFS. By adding a reference mirror with a piezo stage to the setup, we can interfere the scattered field with a plane reference wave. And by moving the mirror in steps, we can change the phase of the reference wave for every line of the raster scan, such that the 2D scan represents a digital off-axis hologram. Applying the standard digital holography reconstruction process, we retrieve a signal that equals the complex far field difference scaled by the reference field amplitude.

Overall, we see consistent signal-to-noise ratio (SNR) improvement over the conventional CFS. For the detection of a polystyrene latex (PSL) particle with a diameter of 60 nm ($\sim \lambda/10$) on a silicon wafer, this new implementation leads to a SNR of 10 dB, which is about 4 dB over the filtered conventional CFS signal. For measurements of a dust particle using a very low amount of incident power (0.0014 mW on wafer), a SNR gain of more than 6 dB is achieved compared to filtered conventional CFS, due to the attenuation of low frequency electronic noises. Therefore, the implementation of SOH improves the sensitivity for detecting small nanoparticles and allows low power applications, such as biological imaging.

Contents

1 Introduction 1

2 Experimental methods 3
2.1 Coherent Fourier scatterometry . . . 4
2.1.1 Standalone setup . . . 4
2.1.2 Detectors . . . 5
2.1.3 Signal to noise ratio . . . 6
2.2 Synthetic optical holography . . . 7
2.2.1 Standalone setup . . . 7
2.2.2 Linearly moving mirror . . . 7
2.2.3 Stepping mirror . . . 8
2.2.4 Reconstruction. . . . 8
2.3 Combined setup . . . 9
2.3.1 Differential signal . . . 10

3 Results & Discussions 11
3.1 Synthetic optical holography phase imaging . . . 12
3.2 Particle detection . . . 15
3.2.1 Simulation . . . 15
3.2.2 Dust particle . . . 17
3.2.3 Low power detection . . . 21
3.2.4 PSL particle 60 nm . . . 23
3.3 Discussions . . . 26

4 Conclusion and recommendations 29
4.1 Conclusion . . . 29
4.2 Recommendations . . . 30

A Appendix 35
A.1 Fourier transform . . . 35
A.2 Derivation of SOH signal . . . 36
A.3 Derivation of differential signal . . . 37
A.4 LabVIEW measurement program . . . 38
A.5 Sample tilt . . . 39
A.6 Through-focus scans . . . 40
A.7 Background noise from reference mirror . . . 42
A.8 Simulation - effect of tilt . . . 43
A.9 Extra supporting results . . . 44

Bibliography 49

1

Introduction

As technology advances and the internet of things rises, the usage of IC chips grows rapidly. Chips that are normally only used in computers can also be found in everyday appliances such as light bulbs, fridges and vacuum cleaners. Furthermore, the rise of self-driving cars which utilize computationally intensive artificial intelligence (AI) and neural networks [20] also drives up the demand for chips. That means the production of semiconductor devices becomes more and more important in the future.

The detection of nanoparticles has been a major problem that semiconductor manufacturers have to deal with. Those nanoparticles can cause major defects in the semiconductor devices [1], therefore the silicon wafers need to be cleaned thoroughly before the fabrication process. This also needs to be done for the reticles or pellicles before exposure. As the state of the art extreme ultraviolet (EUV) lithography process is getting adapted by the industry, which requires very stringent cleaning procedures [31, 36], and the feature size keeps shrinking, the detection of particles is even more important and challenging to ensure yielding. Besides detection, simultaneous localization and classification of the particle without additional setups are often required. The detection system is ideally fast, sensitive and should not damage the wafers with excessive illumination power [29].

The most used scattering based particle detection systems are based on dark-field technique, an example is the Rapid Nano from TNO, the Netherlands. Dark field technique is generally more sensitive than bright field technique, due to the high signal to noise ratio (SNR). However, the high SNR is achieved by using high illumination power [37]. The high amount of energy can be a source of unwanted damage of polymer coatings on a substrate [26].

Coherent Fourier scatterometry (CFS) is a bright field scanning technique that is based on the scattered light from a focused laser beam on the scanned surface. The sample is placed on top of a piezo stage that moves in the lateral directions in order to perform a raster scan. Then a laser beam is focused on the sample, the far field of the reflected light is imaged on a split detector. The difference between the two halves of the split detector gives a voltage value for the current position. If a particle-free surface is scanned, the far field of the laser beam is radially symmetric, thus the differential signal is zero for these positions. However, when the laser is focused onto a particle, the far field becomes asymmetric. This asymmetry is detected as a differential signal that can be either positive or negative, depending on the position of the laser spot with respect to the center of the particle. The size and the position of the particle can be derived from a sequence of differential signals. The performance of this technique is dictated by the signal-to-noise ratio (SNR) of the signal. The scattering cross section decreases when the particle size shrinks [3], as well as the the performance. If one can achieve high SNR, then the accuracy and the sensitivity of the detection will be high. It also means the speed of scan can be increased or illumination power can be reduced, if desired.

There are various techniques that improve the signal-to-noise ratio of CFS, for instance, heterodyne detection [11], inner pupil blocking [29] and radially polarized light [30]. In this thesis, we experiment with a novel technique that has not yet been used before for the application of particle detection, which is the synthetic optical holography (SOH) phase imaging technique. The SOH scan setup is very similar to the Michelson interferometer setup. A laser beam is focused on the sample and a raster scan is performed. The interference of the reflected beam and the reference beam is imaged on a point detector. While the sample surface is being scanned, the reference mirror of the interferometer moves, creating a virtually tilted reference wave due to the phase change per scanned line [33]. The amplitude and the phase can be reconstructed with

standard Fourier filtering. To integrate the SOH phase imaging with the existing CFS setup, a moving mirror can be simply added in the existing setup. We will refer to this new implementation as holographic coherent Fourier scatterometry (HCFS).

In this thesis, we investigate the possible performance gain due to the addition of the phase imaging technique for detecting nanoparticles. The questions we try to answer are

- What extra information can we retrieve by using the HCFS technique?
- How does the signal-to-noise ratio (SNR) of HCFS compare to the conventional CFS?

This thesis is structured as follows. In Chap. 2, we start by showing and explaining the individual setups of CFS and SOH. Following that, our combined setup and theory regarding the extra information are explained. Chap. 3 contains the results and discussions. Lastly, Chap. 4 concludes and summaries the most important results and finalizes with some recommendations.

2

Experimental methods

This chapter contains information regarding the experimental setups and the theory related to them. We first explain the coherent Fourier scatterometry (CFS) technique, as well as the scanning scheme and differential signal associated with it. Then, the basic principles of the synthetic optical holography (SOH) phase imaging technique is explained. Lastly, our setup where two techniques are combined is shown, also we derive an expression for the modulated differential signal.

2.1. Coherent Fourier scatterometry

CFS is a scanning scatterometry technique that has been employed in grating metrology [15, 16, 28] and particle detection [29] for the semiconductor applications. The focus of this thesis is the latter. A CFS setup is similar to that of a confocal laser scanning microscopy (CLSM) [24]. Moreover, CFS is a sensitivity enhancing technique, which focuses on improving the signal to noise ratio rather than the resolution. It has been shown that CFS provides enhancement in sensitivity compared to incoherent optical scatterometry (IOS) [6, 14].

2.1.1. Standalone setup

In Figure 2.1, the experimental setup of CFS is shown, this is the same setup as in [11, 29]. It is very similar to a confocal laser microscope operating in reflection mode. Instead of the image plane, the Fourier plane or the back focal plane of the sample is imaged onto both the camera and the split detector. A HeNe laser with wavelength λ = 633 nm is collimated, linearly polarized and coupled through a fiber. The beamsplitter BS1 directs the laser beam into a microscope objective (NA = 0.9) that is focused on the sample of interest. The sample is placed on a piezo stage (PI P-629.2CD) that can be scanned in the xy-plane. The reflected and scattered light is captured again by the objective and goes back into BS1. Then the transmitted beam is demagnified by a telescopic setup consisting of lenses L1, L2, L3 and beam splitter BS2, before being incident on a camera and a split detector (ODD3W2 BiCell Silicon Photodiode).

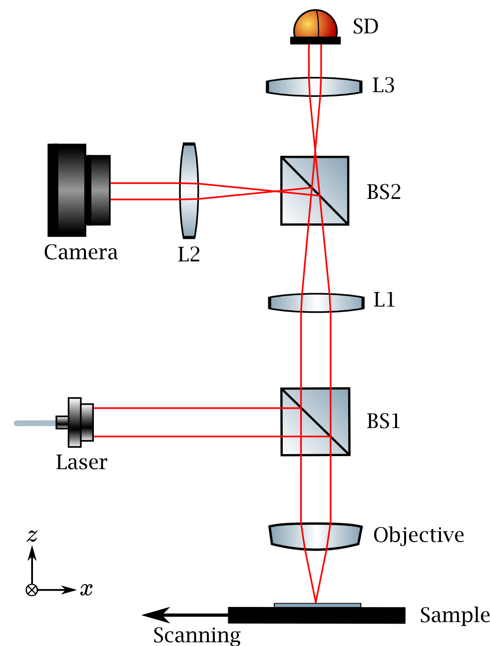

Figure 2.1: Schematic of a coherent Fourier scatterometry particle detection setup. Meaning of the abbreviations: BS - beam splitter, L - lens, SD - split detector.

The raster scan takes place line by line in the x-direction, after each line the stage moves one step up in y, then scans a line in the opposite x-direction. This scanning scheme is shown in Figure 2.2a. Typically, we only keep the lines from left to right as our actual data. Both the control of the stage and data acquisition are handled by one single LabVIEW program.

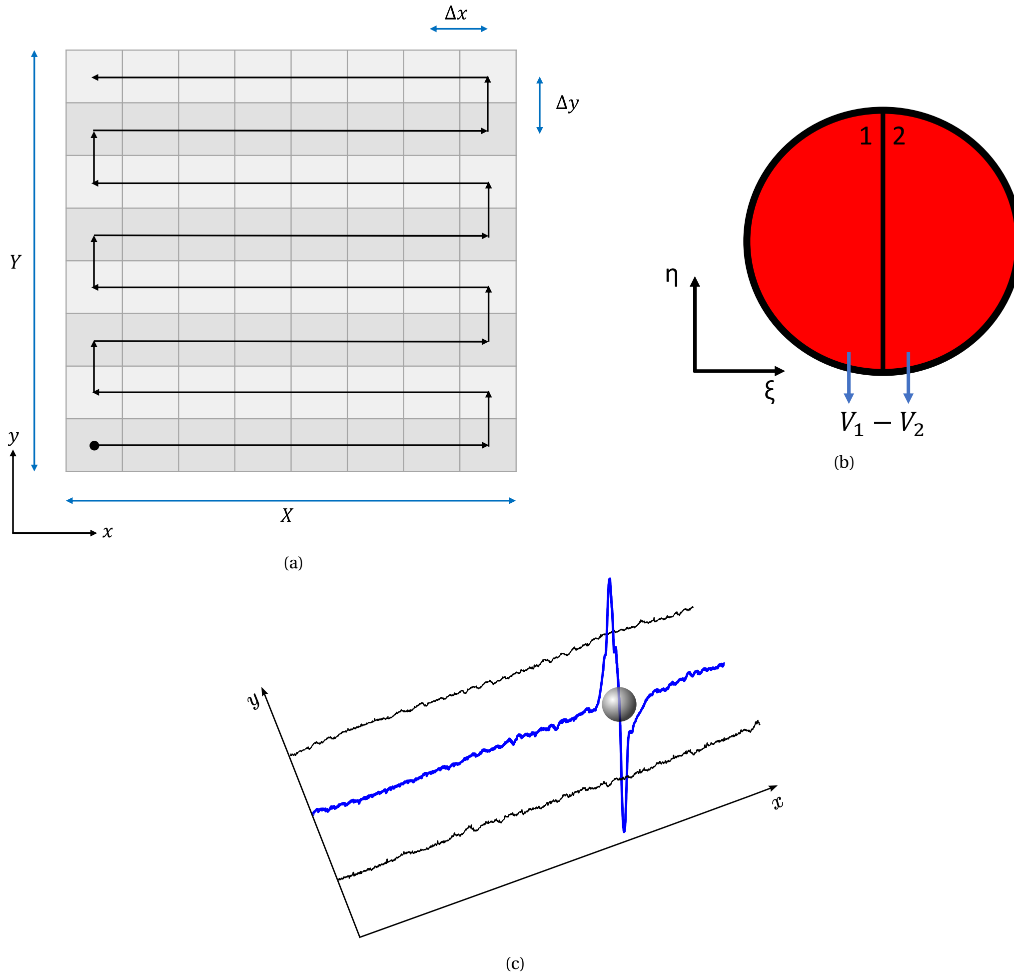

Figure 2.2: (a) The scanning schematic of CFS. The fast axis of the scan is the x-axis and the slow axis is the y-axis. X and Y are the dimensions of the scan area, and Δx and Δy are line widths. (b) Drawing of a split detector where the differential signal is obtained by subtracting the total intensity left with the right. (c) Example of differential line signals, the blue line represents the signal if a particle is scanned and the blacks lines are if a flat surface is scanned. The data are from a measurement of a 20 nm Au particle on Si wafer.

2.1.2. Detectors

In the earliest iteration of CFS setups, a camera or a single pixel detector is used to measure the total intensity at each position. A dip in intensity due to scattering implies the presence of a particle. However, particle detection that uses the differential signals from the split detector shows significant signal-to-noise ratio (SNR) benefits. SNR improvement of two orders is observed in [29]. A split detector, shown in Figure 2.2b, has effectively two pixels, the intensity voltage from the left pixel is subtracted with the right pixel eliminating the majority of noise. The differential signal is described by

$$\begin{aligned} V(\mathbf{r}) &= V_1 - V_2 \propto I_1 - I_2 \\ &= \iint_{D_1} \left|U_S(\mathbf{r},\xi_1,\eta_1)\right|^2 d\xi_1 d\eta_1 - \iint_{D_2} \left|U_S(\mathbf{r},\xi_2,\eta_2)\right|^2 d\xi_2 d\eta_2, \end{aligned} \tag{2.1}$$

where U_S is the scattered field on the detector plane. Coordinates $\mathbf{r} = (x, y)$ give the spatial position on the sample, the coordinates (ξ,η) are for the Fourier plane at each scanned position, and indices 1 and 2 denote the two sides of the detector. This signal gives information about the asymmetry of the scanned surface. If a particle-free surface is scanned, the far field of the laser beam is radially symmetric, thus the differential signal is zero for these positions. However, when the laser is focused onto a particle, typically spherical, the far field changes and becomes asymmetric. The differential signal then becomes non-zero. We display an example of the differential signal in Figure 2.2c. The sign of the signal tells us the location of the laser spot with respect to the center of the particle, the width and the strength of the signal are related to the size of the particle.

2.1.3. Signal to noise ratio

The performance benchmark of the CFS technique is the signal-to-noise ratio, or more accurately the signal-to-background ratio. The scattering cross section is proportional to the particle's size to the sixth power [3]. If the size of the particles gets smaller, SNR decreases as well as the performance. If we can achieve high SNR, then the detection system is more sensitive and we can detect smaller particles. It also means the speed of scan can be increased or illumination power can be reduced, if desired.

In this thesis, we define the signal-to-noise ratio as follows

$$\mathrm{SNR}_{\mathrm{dB}} = 20\log_{10}\left(\frac{\sigma_S}{\sigma_N}\right) \tag{2.2}$$

with σ_S and σ_N the standard deviation of the signal and noise, respectively. This definition emphasises the contrast and does not depend on the offset of the background. On the other hand, SNR computed with the average powers $10\log_{10}(P_S/P_N)$ does depend on the offset. In practice, for a signal with zero-mean background two expressions give a very similar value.

2.2. Synthetic optical holography

The synthetic optical holography (SOH) technique is quantitative method to retrieve the phase information of an object. SOH is suitable for fast and simple phase imaging in scanning optical microscopy [33]. A synthetic optical holography setup is based on the the Michelson interferometer [19] and a confocal microscope [24], and the working principle is based on the off-axis digital holography [25].

2.2.1. Standalone setup

We show in Figure 2.3 a basic configuration of SOH similar to those in [22, 32–34]. The basis of SOH is a laser confocal microscope in reflection mode. A collimated laser beam is split in two arms by a beam splitter. In one arm the laser is focused on the sample by objective L1, which is also placed on a stage, the reflected and scattered light $U_S(\mathbf{r})$ is then again collected by the objective. In the other arm, the reference mirror attached to a piezo stage reflects the light $U_R(\mathbf{r})$ back into the beam splitter. The superposition of the field from both arms is imaged on a single pixel detector by L2, the intensity is then recorded. While the sample is scanned following the previous scheme, the reference mirror moves resulting in a virtual reference phase. The entire recorded image $I(\mathbf{r})$ is a hologram of the sample with a synthetically tilted wave, given by

$$I(\mathbf{r}) = |U_R(\mathbf{r})|^2 + |U_S(\mathbf{r})|^2 + U_S^*(\mathbf{r})U_R(\mathbf{r}) + U_S(\mathbf{r})U_R^*(\mathbf{r}). \tag{2.3}$$

The derivation of this expression can be found in Appendix A.2.

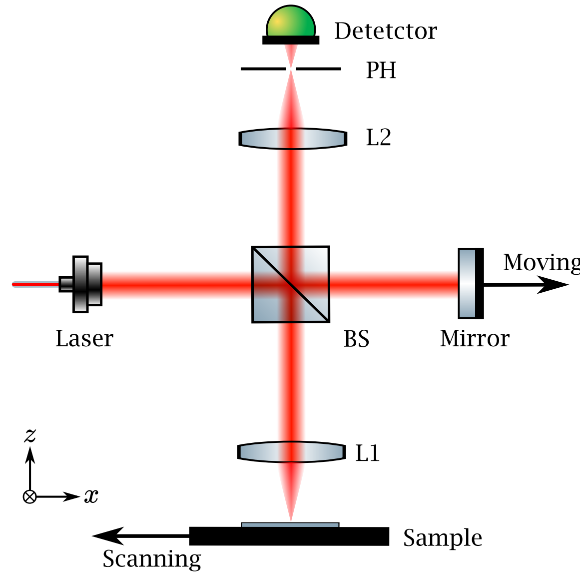

Figure 2.3: Schematic of a SOH phase imaging setup. Meaning of the abbreviations: BS - beam splitter, L - lens, PH - pinhole, SD - split detector.

2.2.2. Linearly moving mirror

In this mode, the reference mirror is moving with a constant speed in one direction. Due to the translation, the reference field $U_R(\mathbf{r}) = |U_R|e^{i\phi_R(\mathbf{r})} = |U_R|e^{i\mathbf{k}_\parallel\cdot\mathbf{r}}$ has a virtual wave vector $\mathbf{k}_\parallel = (k_x, k_y)$ with

$$k_x = \frac{4\pi}{\lambda}\cdot\frac{v_R}{v_x} \quad \text{and} \quad k_y = \frac{4\pi}{\lambda}\cdot\frac{v_R}{\Delta y\cdot v_x/2X}, \tag{2.4}$$

where v_R is the velocity of the mirror, v_x is the scanning velocity in the fast scan direction and X is the scan length in the x-direction as shown in Figure 2.2a [33]. Note that due to the way we scan the sample, time span of a whole line elapses between every acquired line . Therefore, the synthetic wave vector in the slow scan direction k_y is much greater than k_x.

2.2.3. Stepping mirror

Instead of moving at a constant velocity, the mirror can also be moved once per scanned line to create a similar virtual wave vector. Define N as the number of lines or steps that the reference phase is changed by 2π. The position of the mirror at each line is given by

$$d_m = \frac{\lambda}{2} \cdot \frac{m-1}{N} \quad \text{for} \quad m = 1, 2, 3 \cdots . \tag{2.5}$$

Instead of stepping the mirror solely in the positive direction, another option is to cycle the positions every N lines, because fields differ by 2π in phase can be regarded as identical. Therefore, the lth line ($l > N$) corresponds to the mirror position with $m = \text{mod}(l, N)$. In Figure 2.4, position of the mirror for both options are sketched. In theory, they should result in the same virtual reference wave.

The y-component of the resulted virtual wave vector $\mathbf{k}_{\parallel} = \left(k_x, k_y\right)$ is given by

$$k_y = \frac{2\pi}{N\Delta y}, \tag{2.6}$$

while $k_x = 0$. The benefit of this movement over linear movement is the simplicity. By choosing $N \geq 3$, our modulation frequency can never exceed the Nyquist frequency, which is $k_N = 2\pi/(2\Delta y)$. In this thesis, we are mainly utilizing this mirror translation due to the fact that our mirror stage has a relatively short range of 15 um. If we cycle the stepping positions, we will not run out of range during a long scan.

However, the stepping actions may cause stability issues, because the stage accelerates and decelerates rapidly every other line. While by linearly moving the mirror, no acceleration nor forces act on the mirror. To mitigate the stability issues as much as possible, we can program such the stepping of the mirror happens during the lines when the data are not used, so the mirror has a some time to stabilize.

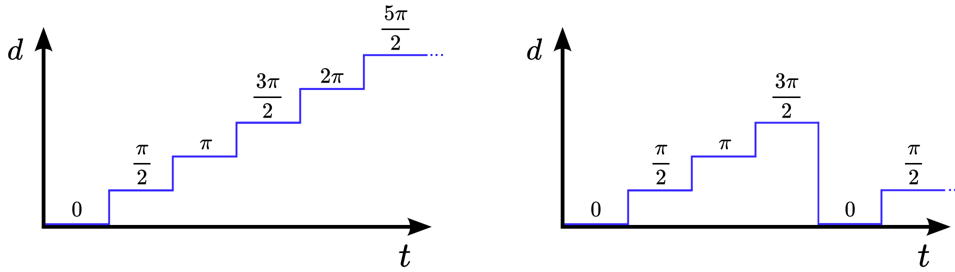

Figure 2.4: Schematic of the mirror position versus time for the N=4 mirror stepping movement. Left: we let the stepping propagate linearly. Right: we cycle the stepping positions in order to overcome range limitation of the stage. The resulting reference phase for each step is indicated on the graphs.

2.2.4. Reconstruction

The reconstruction of a synthetic hologram can be done using standard Fourier transform filtering, identical to the conventional off-axis digital hologram [4, 25]. The Fourier transform of the hologram (eq. 2.3)

$$\tilde{I}(\mathbf{q}) = A(\mathbf{q}) + |U_{\mathrm{R}}|\tilde{U}_{\mathrm{S}}^{*}\left(\mathbf{q}-\mathbf{k}_{\parallel}\right) + |U_{\mathrm{R}}|\tilde{U}_{\mathrm{S}}\left(\mathbf{q}+\mathbf{k}_{\parallel}\right) \tag{2.7}$$

contains the auto-correction term A, the Fourier transform of $|U_{\mathrm{R}}(\mathbf{r})|^2 + |U_{\mathrm{S}}(\mathbf{r})|^2$. The cross term $|U_{\mathrm{R}}|\tilde{U}_{\mathrm{S}}^{*}$ and its complex conjugate are shifted by $\pm\mathbf{k}_{\parallel}$ with respect to the DC-component. We can separate the term $|U_{\mathrm{R}}|\tilde{U}_{\mathrm{S}}$ in the Fourier space, shift it to the center and inverse Fourier transform, then we end up with the complex signal $|U_{\mathrm{R}}|U_{\mathrm{S}}$. For ideal reconstruction, the zeroth order and the first orders should have little overlap in the frequency space, meaning that $\mathbf{k}_{\parallel}$ needs to be chosen wisely.

2.3. Combined setup

To implement interferometer functionality in the CFS setup, we have to simply add a piezo stage (PI P-841.1) with a mirror to our previous setup (see Figure 2.1). Also, an optional 3D printed pinhole can be attached to the mirror to reduce the reference beam size to match that of the scattered beam due to the opening of the objective. Our final setup is displayed in Figure 2.5. One can see that the addition of the SOH technique adds very little complexity to our setup. If we desire to go back to the old setup, we can simply block the reference arm.

This setup is essentially the same as interferometric coherent Fourier scatterometry (ICFS) for characterizing gratings [16]. We shall refer to the combination of CFS with SOH as holographic coherent Fourier scatterometry (HCFS), to distinguish it from the other versions of CFS.

Furthermore, raster scans of the sample and data acquisition are performed in the same way as described previously in section 2.1. Mirror movements that are identical to SOH from section 2.2 are added in the same LabVIEW program, so everything can be controlled from the same place (see Appendix A.4).

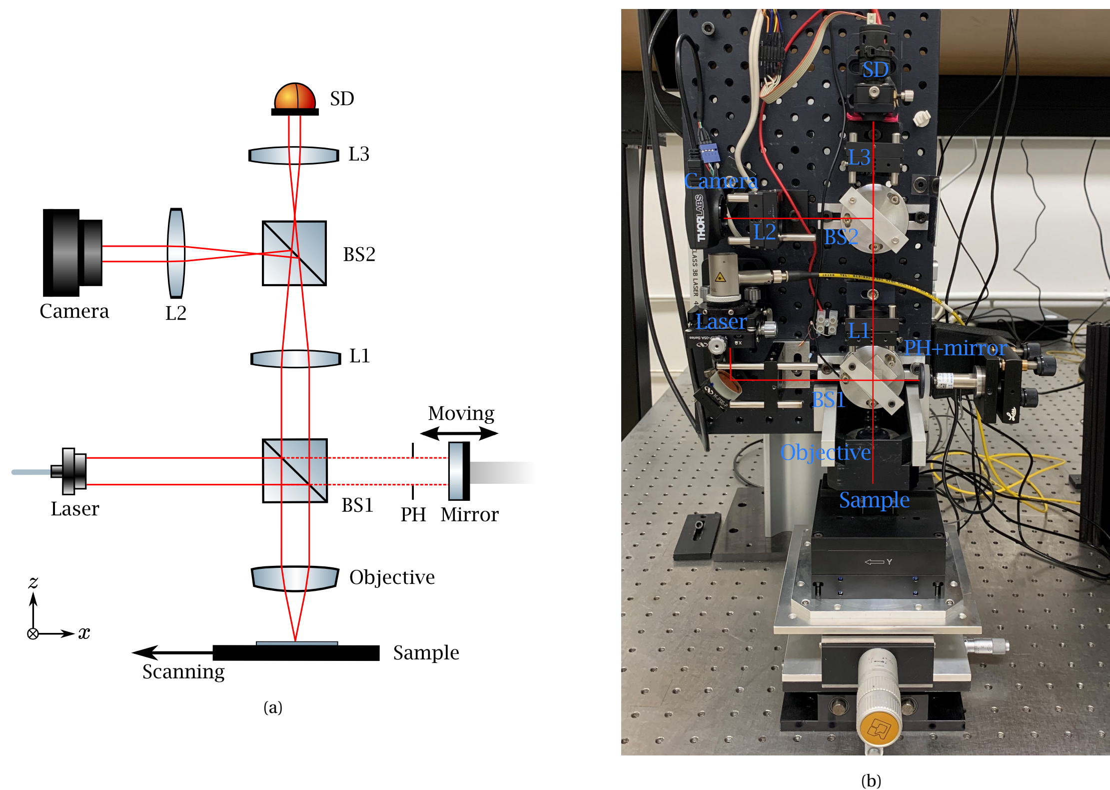

Figure 2.5: (a) Schematic of the combined CFS and SOH setup. (b) Picture of the setup. Meaning of the abbreviations: BS - beam splitter, L - lens, PH - pinhole, SD - split detector.

2.3.1. Differential signal

The implementation of the SOH changes the signal of the split detector. The HCFS differential signal for each scanned position is the integrated intensity difference between the interference pattern on both sides of the detector. It is described by

$$\begin{aligned} V(\mathbf{r}) &= V_1 - V_2 \propto I_1 - I_2 \\ &= \iint_{D_1} \left| U_\mathrm{R}(\mathbf{r}) + U_\mathrm{S}(\mathbf{r}, \xi_1, \eta_1) \right|^2 d\xi_1 d\eta_1 - \iint_{D_2} \left| U_\mathrm{R}(\mathbf{r}) + U_\mathrm{S}(\mathbf{r}, \xi_2, \eta_2) \right|^2 d\xi_2 d\eta_2 \\ &= I_\text{diff,no mirror}(\mathbf{r}) + |U_\mathrm{R}| C^*(\mathbf{r}) e^{i\phi_\mathrm{R}(\mathbf{r})} + |U_\mathrm{R}| C(\mathbf{r}) e^{-i\phi_\mathrm{R}(\mathbf{r})} \end{aligned} \tag{2.8}$$

, where $U_\mathrm{R} = |U_\mathrm{R}| e^{i\phi_\mathrm{R}} = |U_\mathrm{R}| e^{i\mathbf{k}_\parallel \cdot \mathbf{r}}$ the reference field and $U_\mathrm{S} = |U_\mathrm{S}| e^{i\phi_\mathrm{S}}$ the complex scattered field at the split detector, and $I_\text{diff,no mirror}$ the conventional differential signal without the mirror (as in eq 2.1). The complex term $C(\mathbf{r})$ is given by

$$C(\mathbf{r}) = \iint_{D_1} U_\mathrm{S}(\mathbf{r}, \xi_1, \eta_1) d\xi_1 d\eta_1 - \iint_{D_2} U_\mathrm{S}(\mathbf{r}, \xi_2, \eta_2) d\xi_2 d\eta_2, \tag{2.9}$$

which equals the integrated complex field difference between both sides of the detector at every scanned position. The complete derivation of equation 2.8 can be found in Appendix A.3. Note that U_R is assumed to be constant across the whole detector for each scanned position.

The reconstruction can be done in the same way as described in the previous section. The Fourier transform of eq 2.8

$$\tilde{I}_\text{diff,no mirror}(\mathbf{q}) + |U_\mathrm{R}| \tilde{C}^* \left(\mathbf{q} - \mathbf{k}_\parallel \right) + |U_\mathrm{R}| \tilde{C} \left(\mathbf{q} + \mathbf{k}_\parallel \right) \tag{2.10}$$

contains the zero order $\tilde{I}_\text{diff,no mirror}$, which corresponds to the differential signal without interferometer, and two first orders centered at $\pm\mathbf{k}_\parallel$. By Fourier filtering the term $|U_\mathrm{R}|\tilde{C}$, we can retrieve information of complex field differences $C(\mathbf{r})$. It is also noteworthy that this conjugated term contains the constant reference field amplitude $|U_\mathrm{R}|$, while the term $I_\text{diff,no mirror}$ does not depend on it. This means that the strength of the conjugated term $|U_\mathrm{R}|C$ can be controlled, for instance by choosing the reflectivity of the reference mirror. As Si wafer has a reflectivity of approximately 30% [21], the reference field will have a greater amplitude if a highly reflective metallic mirror is used. This way we can presumably improve the sensitivity for detecting particles.

3

Results & Discussions

In this chapter, several results are showcased and discussed. First, we demonstrate the capability of our setup to replicate the SOH phase imaging technique by retrieving the height of a etched micro-structure on a silicon wafer. For particle detection, we start by showing a simple simulation of the HCFS signal from a PSL particle and its reconstruction. Following that, the two sets of result from actual dust contaminants are presented, and the performance of HCFS are evaluated and compared to the conventional CFS. Then, measurement of a 60 nm ($\lambda/10$) PSL sphere is shown and evaluated, also a note is made about the localization of particles. Lastly, all findings above are discussed and elaborated.

3.1. Synthetic optical holography phase imaging

In this section, we demonstrate and verify that our combined setup is capable of performing phase imaging with the SOH technique. A metallic mirror is used with a high reflectivity of approximately 99%, and no pinhole is used.

As demonstration, we use a phase-only etched silicon sample where a letter 'P' has a height of 150 nm. A schematic drawing is displayed in Figure 3.1a. For localization, we first scan the sample using the conventional CFS. In Figure 3.1b, the obtained differential signal is shown. We can clearly recognize the shape of the letter from the outlines. CFS is not an imaging technique, as it is only sensitive to scattering structures. In this case, CFS is sensitive to the edges of the structure, where a jump in height of 150 nm is present. Since the split detector is oriented in the x-direction, orthogonal edges (in y) give a stronger signal than the parallel edges. Additionally, the width and amplitude of the signal depends on the sidewall angle and height of the etching. Hence, CFS is also a suitable method for characterizing structures for semiconductor applications, although it is not the focus of this thesis.

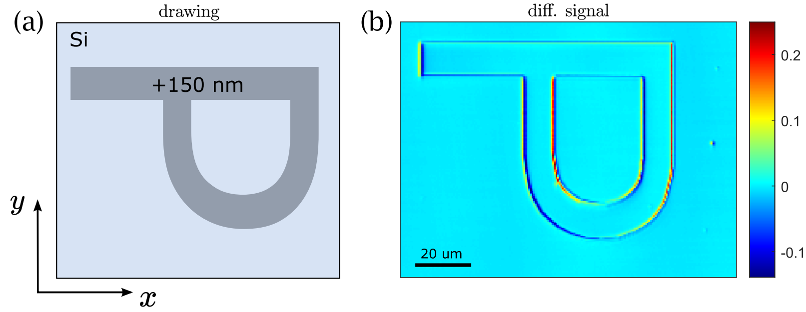

Figure 3.1: **(a)** A drawing of the silicon sample with a letter 'P' etching of 150 nm. The length of the letter is about 100 um. **(b)** The intensity measurement with the conventional differential CFS, (210×160 pixels, 120×100 um^2, imaging time 120 seconds).

As our setup is equipped with a split differential detector instead of a single pixel detector, a change is needed to replicate the SOH technique. We can replace the split detector or use additional electric circuits to sum up the voltage from both sides. But instead, we obtain the sum signal by simply shifting the detector to one side, such that the whole beam is captured by one single pixel (Figure 3.2), thus requiring very little modification to the setup.

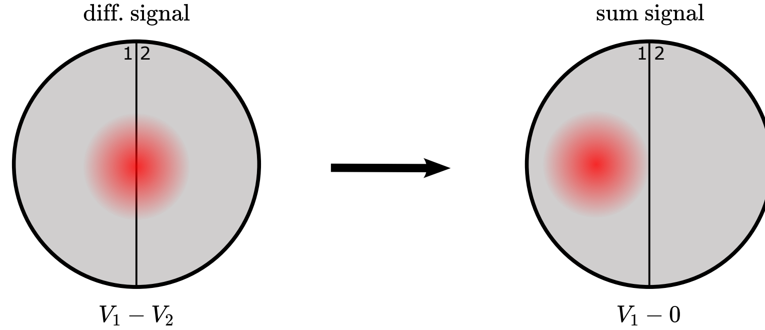

Figure 3.2: Drawing of a split detector. On the left, we center the laser beam, the output equals the differential signal. On the right, we shift the detector to one side, the output is the signal from the entire beam intensity.

Next, we scan using our implementation of SOH with the mirror stepping option $N = 4$, i.e. every 4 lines the reference phase changes by 2π. A schematic of the phase map can be seen in Figure 3.3a. The recorded hologram I, shown in Figure 3.3b, exhibits a fringe pattern where the signal maxima repeat every 4 lines. However, modulation in the x-direction can also be observed, this is explained by a small tilt of the sample plane. This tilt results in a shift of the two first orders, thus can be completely removed during the reconstruction process in theory.

The Fourier transform of the hologram (Figure 3.3c) contains clearly 3 orders as we expect. In order to reconstruct the phase of the object, we apply a Gaussian window to the Fourier spectrum indicated by the red dotted circle, followed by shifting it to the center and taking the inverse Fourier transform. The full width at half maximum (FWHM) of the Gaussian window equals the diameter of the red circle.

The reconstructed amplitude of the object is displayed in Figure 3.3d and the phase in e. The phase is unwrapped with a unwrap algorithm [8, 10]. The phase image shows phase drift, mainly in the y-direction, caused by the instabilities of the interferometer due to vibrations, air turbulence and thermal expansions, introducing changes of the phase difference between the scattered field and reference field [33]. Also, the phase image exhibits some artifacts near the edges. Some phase distortions are present at the upper part of the image and the inner part of the 'P', which are caused by the wrapping of the phase, as a result the phase is offset by a factor of 2π. With the phase, we can calculate the height profile of the sample using the equation

$$h(x,y) = \frac{\lambda}{2\cdot 2\pi}\phi_S(x,y). \tag{3.1}$$

We also apply some post-processing to the height profile to remove the artifacts. We first trim off the edges to get rid of the artifacts. Then we line-wise subtract a straight line obtained from data at the left and right end of each line and assign both ends a value of 0. Each line is also median filtered to remove spikes at the edges of the structure, yielding a correct height profile (Figure 3.3f).

Furthermore, we can compute the average height of the structure by applying a mask of the shape of the letter 'P' (Figure 3.3g), the mask is acquired by taking data points between 100 and 200 nm of the entire surface profile. Averaging the entire letter 'P' area, we found 145.3 nm as the average height, which deviates to the theoretical value of 150 nm by only 3%. So we have shown the SOH technique is quantitatively accurate for height profiling of an uniform structure, even though our setup is not well optimized.

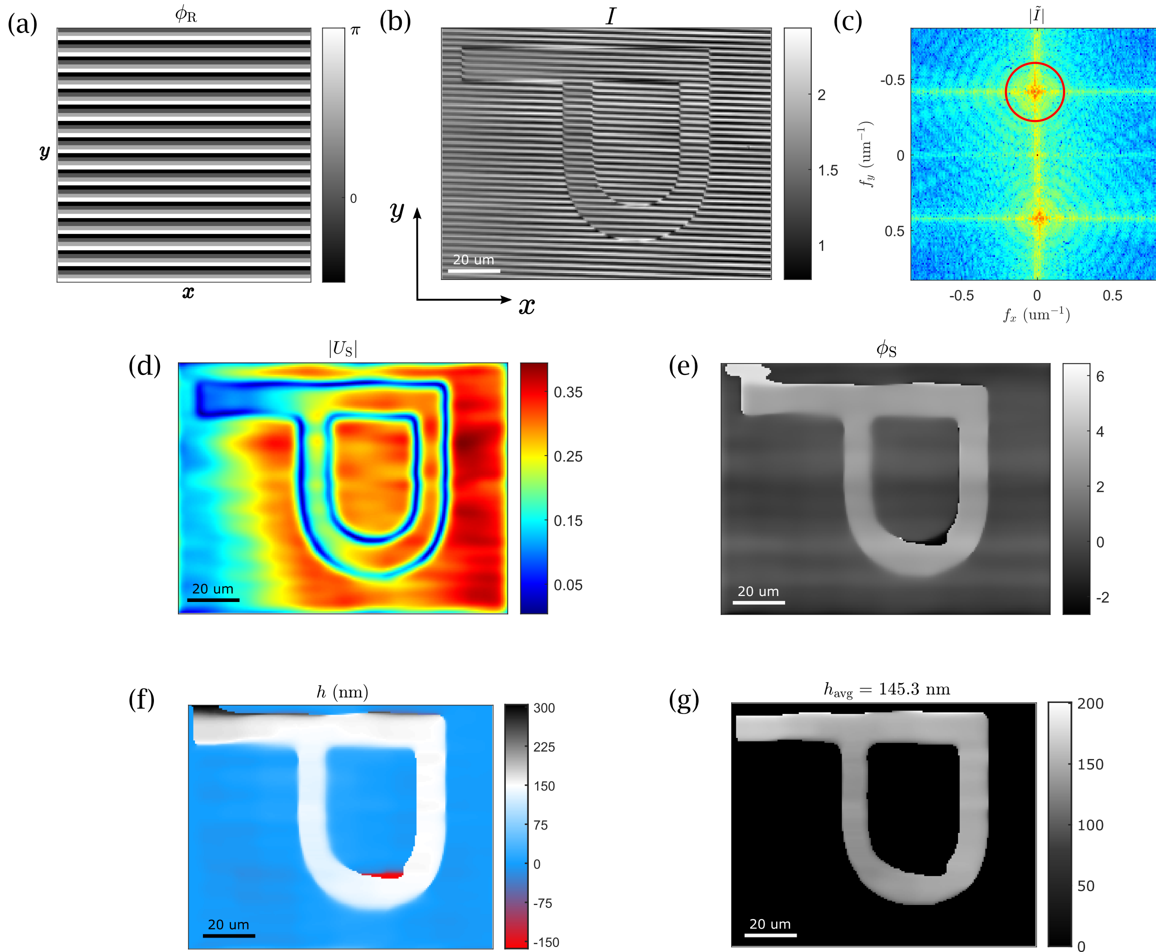

Figure 3.3: **(a)** The reference phase map ϕ_R of the scan, where every 4 lines the phase changes by 2π. The number of lines shown does not equal the actual scan. **(b)** The intensity of the hologram obtained from the raster scan, (210×160 pixels, 120×100 um^2, imaging time 120 seconds). **(c)** Amplitude of the Fourier transform of the recorded hologram (log scale). A Gaussian filter is used for Fourier filtering, where the FWHM is indicated by the red circle. **(d)** The amplitude of the reconstruction. **(e)** The unwrapped phase of the reconstruction. **(f)** Post-processed height profile in nm. **(g)** Height profile after applying a mask for the letter 'P', the average height of the structure is 145.3 nm.

Sample tilt

We have noticed a tilt in the sample from the change of the interference pattern during the raster scan. The pattern changes constantly while a line is scanned, implying a constant phase change. Looking at the hologram (Figure 3.3c), we can see the intensity varies sinusoidally within one line. Furthermore, the right part of the image has a higher average intensity than the left part, implying the presence of defocus due to tilt.

If the tilt is small, the SOH technique is in theory able to get rid of the tilt completely during the Fourier reconstruction process. The tilt adds a phase ramp to the scattered field $U_S \to U_S e^{i\mathbf{k_t}\cdot\mathbf{r}}$, in the Fourier transform of the hologram the two first orders are simply shifted by $\pm\mathbf{k_t}$. In Figure 3.3d, we indeed can see the first orders are not centered in the x-direction.

An attempt is made to minimize this tilt, which is presumably caused by the tolerance of the sample holder blocks. We place a few pieces of paper underneath the sample stage to counteract the tilt. However, the perceived tilt on the interferometer when scanning remains quantitatively identical with or without the paper. We are yet unable to explain this phenomenon. More details can be found in Appendix A.5. In the following parts of this thesis, we still have to deal with this tilt. However, if we scan smaller areas, the effect of the tilt should become less noticeable.

Some other limiting factors and sources of error are: the stability of the Michelson interferometer, external vibrations and air turbulence, stability and precision of the mirror piezo stage and aberration of the high NA optical setup.

3.2. Particle detection

3.2.1. Simulation

In order to understand the behaviour of the differential signal, we start with a simple simulation of HCFS for detecting a spherical polystyrene latex (PSL) particle.

First, one line of complex scattered far fields with linearly polarized incident light is generated by a finite-difference time-domain method (FDTD) [17], provided by D. Kolenov. The field amplitude of two data points are shown in Figure 3.4. To save computational time, this line is repeated multiple times in the y-direction. Then the differential signal is generated by dividing the field in two halves and subtracting their intensities with each other. Consequently, a 2D cosine squared window is applied on top of the signal replicating a spherical particle. At last, we apply a zero padding to the signal simulating the flat surface of the substrate around the particle.

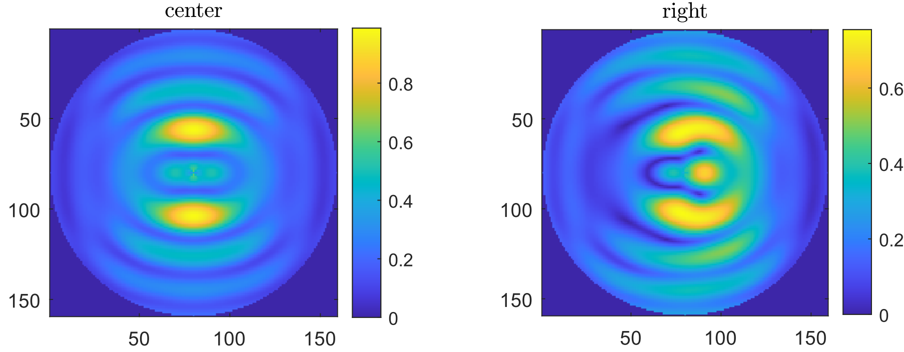

Figure 3.4: Amplitude of scattered far fields of a particle from the simulation using linear polarized light. Left: the laser beam is focused on the center of the particle, so the field is symmetric w.r.t the left-right halves. Right: the laser beam is focused on the right side of the particle resulting in a left-right asymmetric field. The units of the axes are pixels.

The simulated signal from the conventional CFS (using eq. 2.1) is displayed in Figure 3.5a, the signal contains two opposite peaks and a zero crossing at the center of the particle as expected.

Next, we introduce a reference phase corresponding to the stepping mirror with $N = 4$, i.e. each line has a constant phase and every 4 lines the reference phase changes with 2π. The modulated differential signal can be generated using eq. 2.8, which is shown in Figure 3.5b. The particle signal exhibits fringe behaviour as we expect. The background is again padded with zero, because in theory the interference pattern remains symmetrical when scanning a flat surface. Taking the Fourier transform (Figure 3.5d), we clearly see three orders, the zero order at the center and the - and $+1^{st}$ order at the upper and lower halves.

By reconstructing the zero order with a rectangular window, we retrieve the exact signal (Figure 3.5e) as the conventional CFS technique. To reconstruct the complex term C, we apply a rectangular window to the upper plane, shift the result to the center and take the inverse Fourier transform. The amplitude of this complex term C is shown in Figure 3.5f, together with the real and imaginary component in Figure 3.5g and h, respectively. Looking at the real and imaginary part, we see a similar differential signal as the signal with no mirror, however lower in amplitude. Two peaks with opposite signs are located at the sides of the particles and a zero crossing occurs at the center. Note the complex term C is scaled by the amplitude of the reference field, meaning that we can in theory boost this first order signal by using a stronger reference beam. In this case, the scattered fields are normalized and the reference field amplitude $|U_{\mathrm{R}}|$ equals 1.

The phase, which is the argument of the complex differential term C is shown in Figure 3.5i. We can see an anti-symmetrical behaviour and a discontinuity at the center of the particle. The background signal, which has amplitude of 0, exhibits a chaotic phase behaviour due to numerical errors. Therefore, we can not utilize this phase information to distinguish particles. Despite that, if we can identify the particle through the differential signals, we can possibly utilize the discontinuity to determine the center position of the particle w.r.t. the position of the laser beam on the surface.

So far, we have shown that HCFS gives us additional information while preserving the original CFS information.

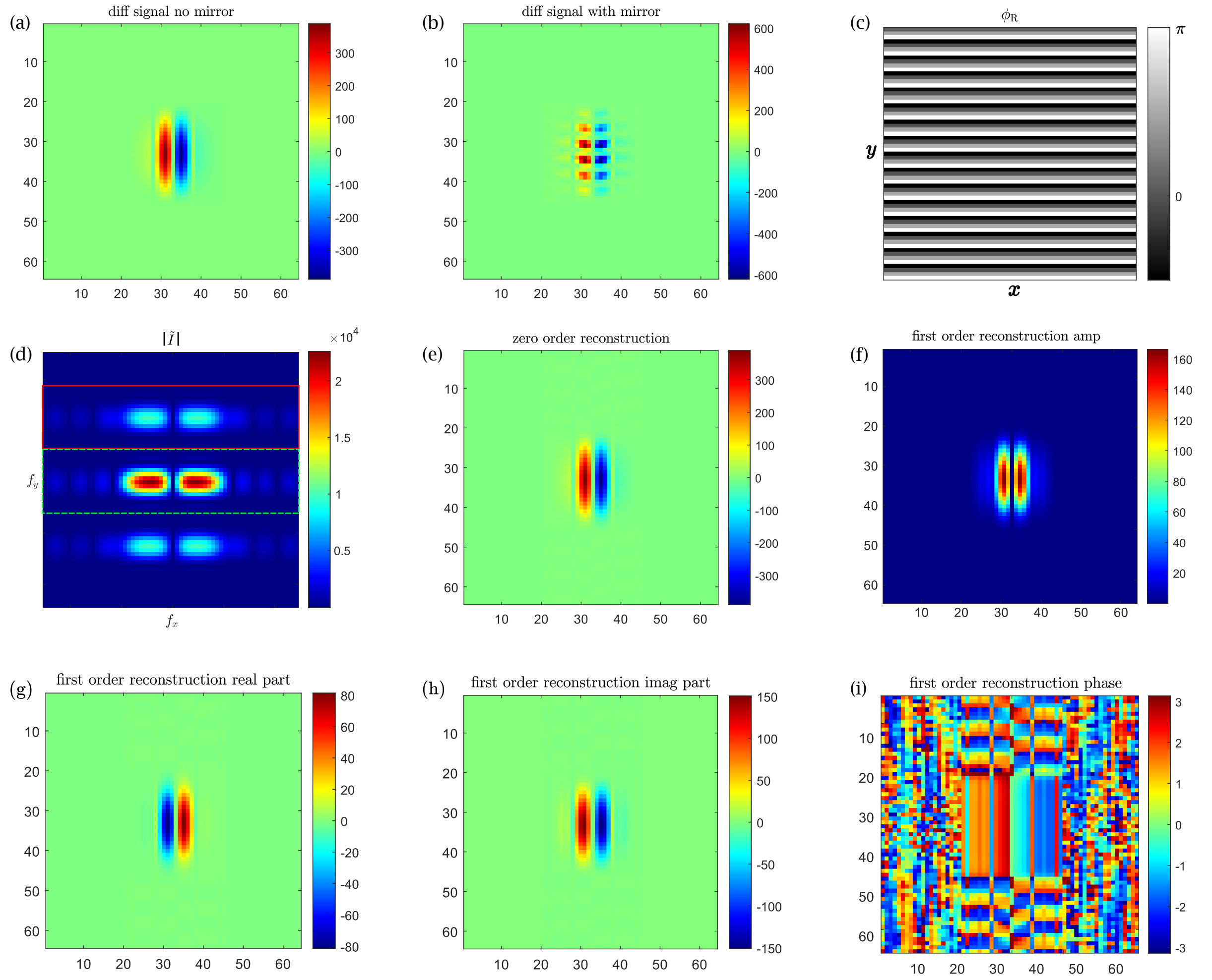

Figure 3.5: **(a)** Simulated differential signal of a particle with the conventional CFS. The units of the both axes are pixels (64x64 pixels), the unit of the signal is an arbitrary unit of voltage. **(b)** Simulated differential signal of a particle with HCFS. **(c)** The reference phase map ϕ_R of the synthetic reference wave, where every 4 lines the phase changes by 2π. **(d)** Amplitude of the Fourier transform of the signal in (b). **(e)** The reconstructed signal of the zero order Fourier spectrum using a rectangular window indicated by the green dashed rectangle in (d). The first order Fourier spectrum is reconstructed using a rectangular window indicated by the red solid rectangle, the amplitude of the reconstruction is shown in **(f)**, the real part is shown in **(g)**, the imaginary part is shown in **(h)** and the phase is shown in **(i)**.

3.2.2. Dust particle

In this section, we measure a spherical dust particle on a wafer with moderate incident power (0.012 mW on the wafer) and evaluate the performance between CFS and HCFS. Again a highly reflective metallic mirror is used without a pinhole.

Focus

First we may make a note on focusing. As we are using a high NA objective (NA=0.9) with a focal distance of ca. 100 um, meaning a relatively low depth of focus [18]. In our case, the depth of focus is approximately 560 nm. So maintaining proper and consistent focus during different scans is important, because the focus affects the amplitude and shape of the signal. Previously, the method for achieving good focus is by first estimating the focus position z_0, followed by measuring a (known) particle numerous times while varying the focus depth z. The imbalance of the differential signal ($|I_{\max}| - |I_{\min}|$) versus position z can be plotted as a S-curve, where the zero-crossing gives the best focus [12]. However this procedure is tedious and time consuming. With the implementation of SOH technique, we can use the reference mirror as a tool to focus. If the beam is focused on the surface of a Si substrate, the interference pattern of the reflected and the reference beam tells us about the phase of the reflected beam, assuming the reference is a plane wave. Defocus seen as aberration gives radially symmetric quadratic phase shift in the form of $2r^2 - 1$ [2]. On the left of Figure 3.6, we can clearly see a fringe pattern corresponding to the phase profile of defocus, so we assume the beam is out of focus. Minimizing the fringes, as shown on the right of Figure 3.6, is a quick way to get good focus. With a few through-focus scans (Appendix A.6), we found this method gives us ±100 nm (±λ/6) accuracy of focusing. Although not guaranteeing the sharpest focus, this is a fast and consistent method for focusing, especially useful when changing samples.

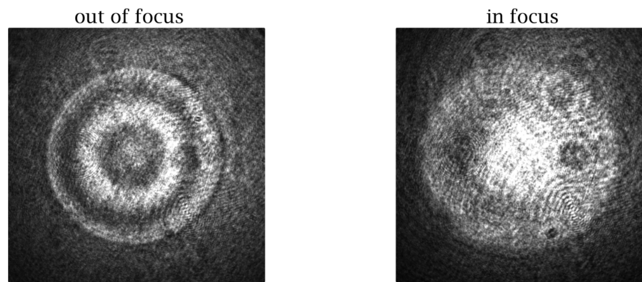

Figure 3.6: The interference pattern on the camera for determining the focus. Left: there are fringes corresponding to defocus aberration. Right: minimized fringes, we assumed the beam is in focus.

Measurements

After localizing an isolated particle, a few scans are done with the conventional CFS technique as a point of reference. An example is shown in Figure 3.7, where we can clearly see a circular shaped particle and the signals left to right are opposite with respect to each other. The area of this scan is 75×12 um^2, where 300 lines are acquired in 90 seconds. As a moderate amount of incident power is used and the size of this particle is relatively large, the SNR of this scan is about 20 dB. Although not necessary for this particle, we will still seek possible SNR improvement by using HCFS.

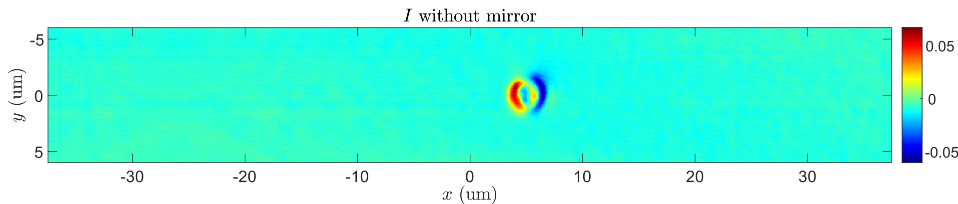

Figure 3.7: Measured differential signal of a dust particle with the conventional CFS, (1500×300 pixels, 75×12 um^2, imaging time 90 seconds). The unit is Volt.

Next, we unblock the reference mirror and apply the stepping movement with $N = 4$, where every 4 lines the reference phase changes by 2π. With the same raster scan, we obtain the hologram image shown in Figure 3.8a. The zoom (Figure 3.8b) shows a clear fringe pattern on the particle. However, the background

also exhibits a fringe pattern. Although, the background should be uniform and have value zero in theory. The cause is the slightly asymmetrical interference pattern at the split detector due to aberrations and beam non-uniformity, as seen in Figure 3.6.

The Fourier transform of the hologram, $|\tilde{I}|$ (Figure 3.8c), contains clearly 3 orders. The frequencies in the center correspond to the signal without a reference mirror $\tilde{I}_{\text{diff,nomirror}}$. Two first order terms at the upper and lower halves of the Fourier plane correspond to $|U_\text{R}|\tilde{C}$ and $|U_\text{R}|\tilde{C}^*$.

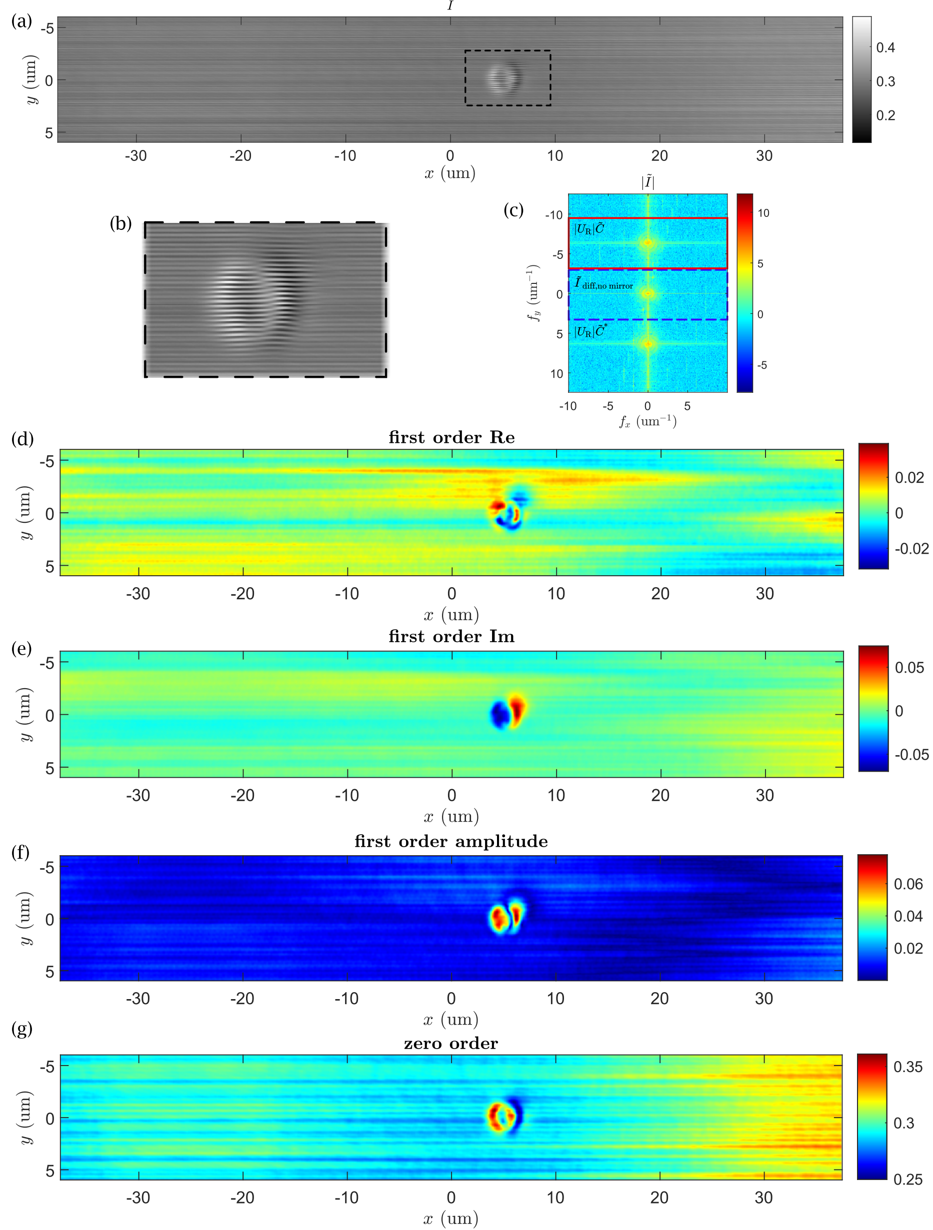

Figure 3.8: **(a)** Measured differential hologram I of a particle with HCFS, (1500×300 pixels, 75×12 um^2, imaging time 90 seconds). **(b)** Zoom into the particle region outlined by the dashed square in (a). **(c)** Amplitude of the Fourier transform of the signal in (a), logarithmic scale. **(d)** Real component, **(e)** imaginary component and **(f)** amplitude of the first order reconstruction with a cosine window indicated by the solid red rectangle in (c). **(g)** The reconstructed signal of the zero order Fourier spectrum using a cosine window indicated by the blue dashed rectangle in (c).

Cosine filter

To reconstruct the first order signal, we first try applying a 2D cosine window to the upper plane, indicated by the solid red rectangle, followed by shifting and inverse Fourier transform. This cosine window is of first order in f_y-direction and second order in f_x-direction, i.e. $W_\text{cosine} = \cos(af_x)^2\cos(bf_y)$, a surface plot is displayed on the left of Figure 3.9. The reconstructed first order signal is a complex quantity, in Figure 3.8d-f we show

the real part, imaginary part and the amplitude of the reconstruction. The imaginary part appears quite symmetrical, but the real part seems distorted. However, the first order signals might not always look like the zero order signals, because the phase of the field is a major factor. Another explanation is aberration, e.g. tilt, defocus, spherical aberration, as any phase changes of the scattered field will affect this complex signal. As we don't know the exact material and shape of this particle and have no simulation data of it, no conclusion can be derived here. Furthermore, we see that the background still contains some fringes, which will greatly affect the SNR, especially when detecting weaker scattering particles. In the same manner, we can also reconstruct the zero order signal (Figure 3.8g), which is the same as the conventional CFS signal as expected, but with a distorted background.

The mirror movement and mechanical instabilities are the main cause of the error. As noise measurement, we launch a scan with the sample stage being fixed and the mirror moving (details in Appendix A.7). We see that the majority of the noise has a low frequency component in the x-direction, located vertically in the center of the Fourier plane. The Fourier transform of the signal from a particle contains mainly non-zero x-frequencies, e.g. in Figure 3.5d from the simulation. We intend to use a low cut filter to remove the low x-frequencies, and superimpose it on the existing cosine window, yielding a band pass filter. On the right of Figure 3.9, the center cross section of this band pass filter is shown.

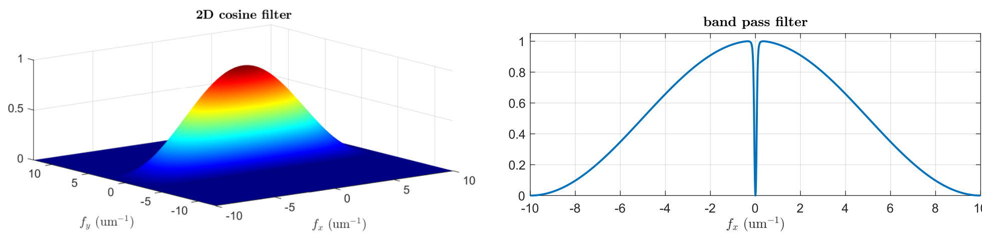

Figure 3.9: Left: surface plot of the cosine window for Fourier reconstruction. Right: center cross section in f_x of the band pass filter obtained by combining the cosine window with a high pass filter.

Band pass filter

Repeating the reconstruction process with the new filter, we can see the reconstructed first order images have an uniform background (Figure 3.10a-c). The same can be said for the zero order (Figure 3.10d), also the shape of the signals is kept intact. As reference, we also enclose in Figure 3.10e the result from the conventional CFS and in f the filtered version using the same filter as the others. In order to see whether there is a gain in SNR, we compute the SNR for each plot by using a circular mask that defines the signal portion, the same mask is used for all plots. By filtering the reference signal, we see a SNR gain of more than 6 dB. The imaginary part out of the first orders has the highest SNR in this case. Compared to the reference (e), there is almost 10 dB of gain in SNR. And compared to the reference after filtering (f), a gain of more than 3 dB is achieved. Additionally, the first order signal has a higher peak-to-peak value or amplitude than the conventional CFS, because this cross term $|U_\mathrm{R}|C$ contains the relatively strong reference field amplitude. Note that the zero order reconstruction (d) has a lower SNR with regard to the filtered reference scan (f). This is due to the additional noise caused by the instabilities of the reference mirror.

In Tabel 3.1, we show the SNR values for 3 scans of HCFS and 3 scans of conventional CFS on the same particle. Compared to unprocessed data from conventional CFS, the HCFS improves the SNR up to 10 dB. If we apply the same (noise) filtering to that data, there is still a gain up to 3 dB. Furthermore, the (statistical) average gain is computed to be 2.2 dB, the gain here is defined as the difference between the highest SNR signal of HCFS (***highlighted***) and the filtered signal of conventional CFS.

Table 3.1: Signal-to-noise ratios for 3 scans of HCFS and 3 reference scans on the same particle. Also the (statistical) average gain compared to filtered reference scans is computed. The results of the extra two sets of scans are shown in Appendix A.9.

	scan #1	**scan #2**	**scan #3**
SNR (dB) first order Re	22.11	24.57	***29.42***
SNR (dB) first order Im	***30.73***	***28.46***	19.89
SNR (dB) zero order	24.31	24.10	23.91
SNR (dB) reference	20.78	20.44	20.48
SNR (dB) reference filtered	27.26	27.11	27.54
average gain (dB)		2.23	

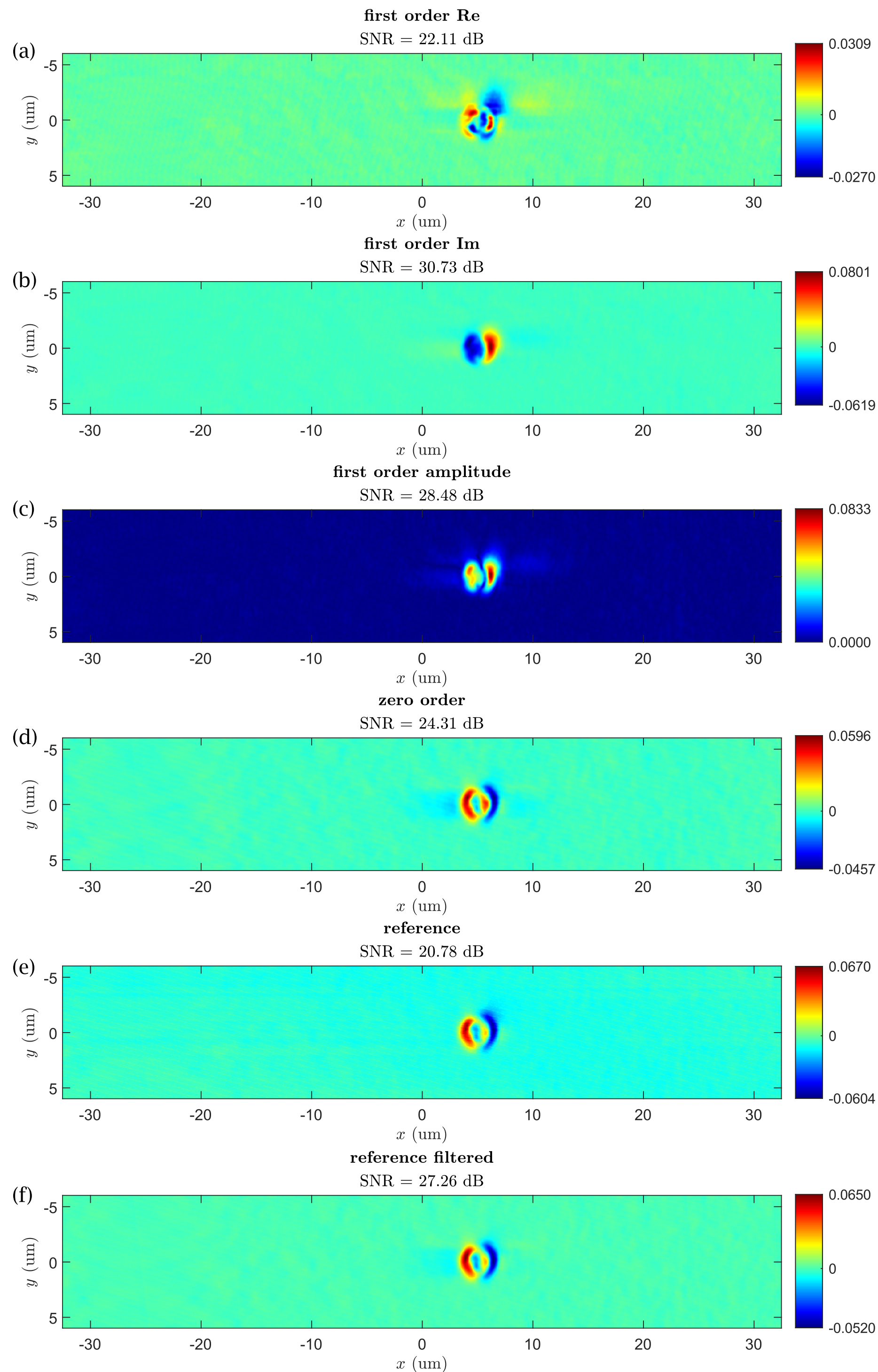

Figure 3.10: Using the band pass filter: **(a)** the real component, **(b)** the imaginary component and **(c)** the amplitude of the first order reconstruction. **(d)** The zero order reconstruction. **(e)** Signal of the conventional CFS without filtering. **(f)** Signal of the conventional CFS after filtering with the band pass filter. For each plot, 5 um of data are removed from both sides of x to eliminate the scanning artifact, then SNR are computed and shown.

In this section, we have shown the HCFS measurement of a dust particle. We introduced a band pass filter which drastically improves the reconstruction compared to a regular low pass filter. The first order signal using HCFS has a higher amplitude and a SNR gain of up to 3 dB compared to the conventional CFS with noise filtering.

3.2.3. Low power detection

In this section, we lower the incident power by roughly one order of magnitude, to 0.0014 mW on the wafer, and measure another dust particle. Then, we will evaluate HCFS's performance compared to the conventional CFS.

We begin by measuring the particle with the conventional CFS as reference, this is shown in Figure 3.11a. We can see the signal is quite weak, as the signal amplitude is linear to the power. In the background, we can see some periodic noise of different frequencies. So at this power level and particle size, we can say that the measurement is limited by the electronic noise. The signal-to-noise ratio is only about 7 dB.

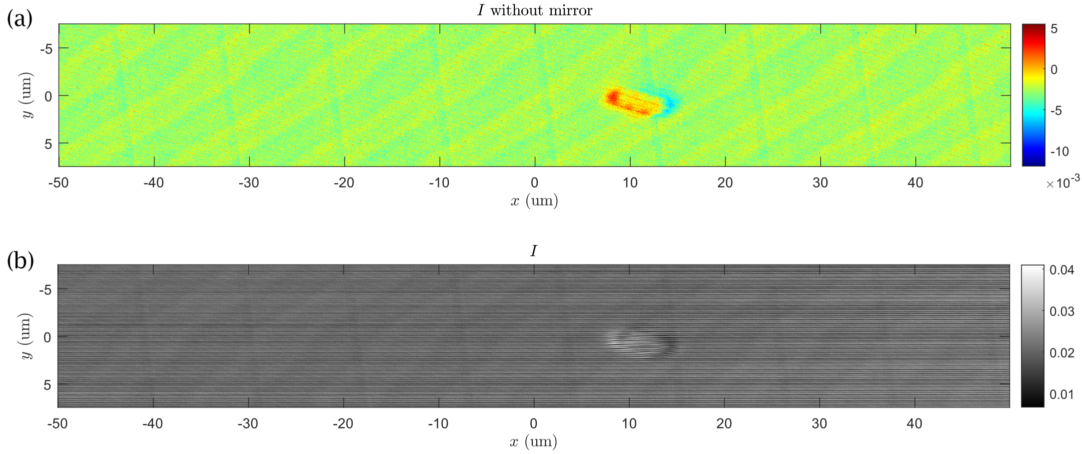

Figure 3.11: **(a)** Conventional CFS and **(b)** HCFS measurement of a dust particle with low incident power, (1500×300 pixels, 100×15 um^2, imaging time 90 seconds).

Next, using HCFS with $N = 4$ mirror stepping movement, i.e. every 4 lines the reference phase changes by 2π, we recorded the hologram I (Figure 3.11b). Applying the same Fourier reconstruction process as in the previous section, the results are shown in Figure 3.12 together with their SNR. Also, we included the results of the conventional CFS before and after noise filtering as a point of reference. Again, the reconstructed zero order signal (d) is identical to the conventional CFS as expected. Not only that, the SNR is comparable to the reference post filtering (g). On the other hand, the first order signal (a) has a SNR of 8 dB higher than the zero order. We can see that the background fluctuation of the zero order is huge compared to the first order. The main reason is that the first order signal gets rid of the $1/f$ noise of the electronic components (typically < 200 Hz), electrical interference and cross-talk (50 - 60 Hz), similar to the heterodyne detection [11]. However, weaker high frequency electronic noises are aliased in the first order as lower frequencies, as seen in Figure 3.12e.

To illustrate the consistency, we again list the SNR values for 3 scans of both HCFS and conventional CFS in Tabel 3.2. Compared to raw CFS data, we improve the SNR by up to 15 dB with HCFS. Even compared to the noise filtered CFS data, we achieve a significant SNR gain of up to 8 dB.

Table 3.2: Signal-to-noise ratios for 3 scans of HCFS and 3 reference scans on the same dust particle. Also the (statistical) average gain compared to filtered reference scans is computed. The gain here is defined as the difference between the highest SNR signal of HCFS (***highlighted***) and the filtered reference signal. The results of the extra two sets of scans are shown in Appendix A.9.

	scan #1	**scan #2**	**scan #3**
SNR (dB) first order Re	***22.52***	18.24	***19.02***
SNR (dB) first order Im	21.57	***19.77***	17.01
SNR (dB) zero order	14.57	14.17	13.60
SNR (dB) reference	7.35	7.28	6.89
SNR (dB) reference filtered	14.24	14.18	13.79
average gain (dB)		6.37	

We have shown hereby that the HCFS technique is very suitable for detecting particles with low incident power, where the signal strength is comparable to the electronic noise. This means HCFS is also suitable for the application of biological imaging, where excess power can damage the specimen.

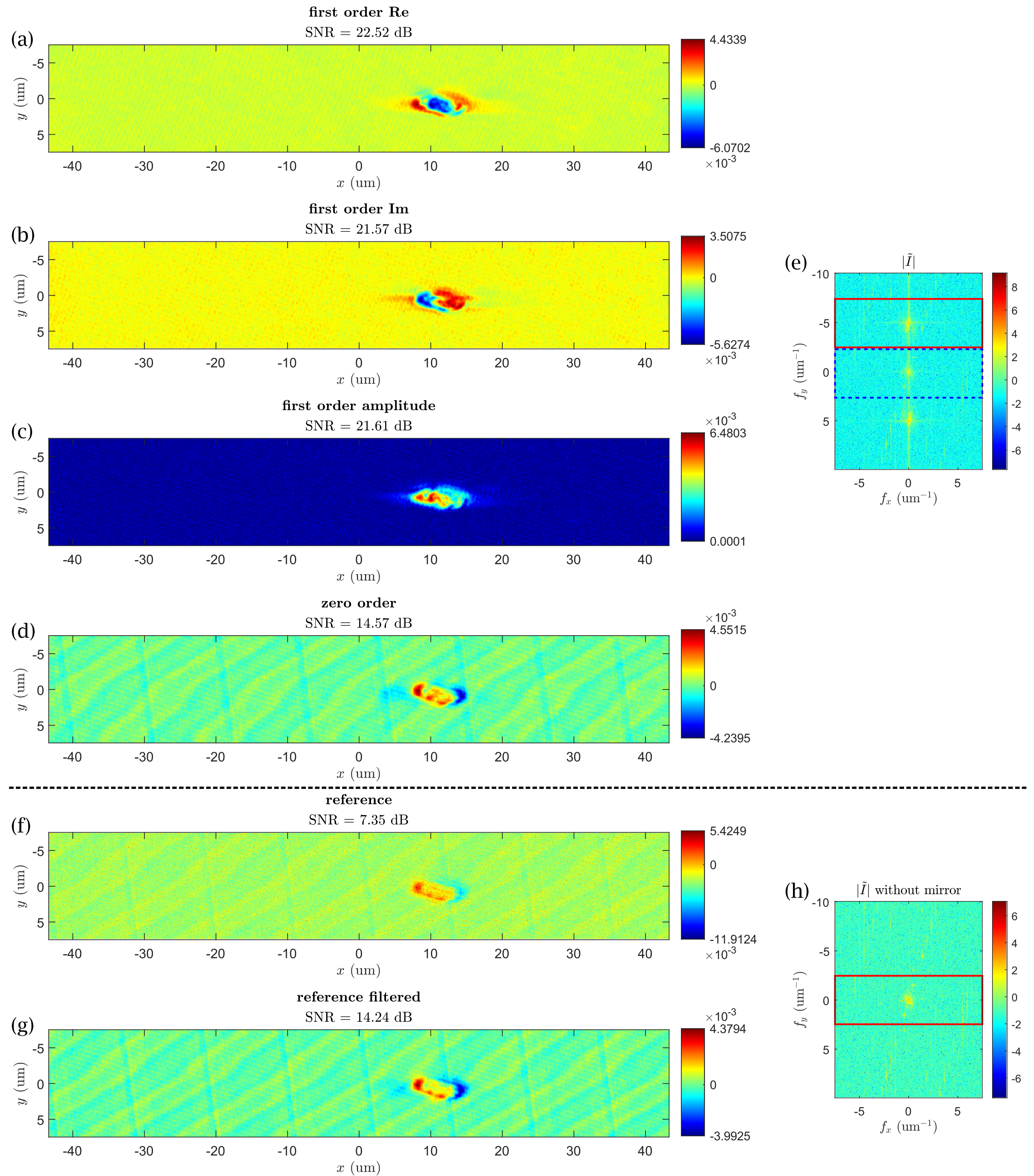

Figure 3.12: **(a)** The real component, **(b)** the imaginary component and **(c)** the amplitude of the first order reconstruction. **(d)** The zero order reconstruction. **(e)** Amplitude of the HCFS signal in logarithmic scale. The solid red window indicates the first order, and the dashed blue window indicates the zero order. **(f)** Signal of the conventional CFS without filtering. **(g)** Signal of the conventional CFS after filtering with the band pass filter. **(h)** Amplitude of the conventional CFS signal in logarithmic scale. The solid red window indicates where the filter is applied. The exact same band pass filter is used for each Fourier filtering step. For each plot, 6.7 um of data are removed from both sides of x to eliminate the scanning artifact, then SNR are computed and shown.

3.2.4. PSL particle 60 nm

In this section, we measure a polystyrene latex (PSL) nanosphere with a diameter of 60 nm ($\sim \lambda/10$) using 0.016 mW of incident power on the Si wafer. In this case, we are using a pinhole on the mirror to reduce the size of the reference beam in order to reduce background fluctuations. Again we evaluate the performance between CFS and HCFS.

We start by showing a measurement of the particle using the conventional CFS technique, which is displayed in Figure 3.13a. As the scattering cross section varies with the sixth power of the scatterer size [3], we see that the SNR of the particle is low ($\approx$ 2.6 dB) even with relatively high incident power. It is below the requirement for surface inspection in the semiconductor industry of 3 dB [9]. For clarification, the particle location is indicated by the red circle.

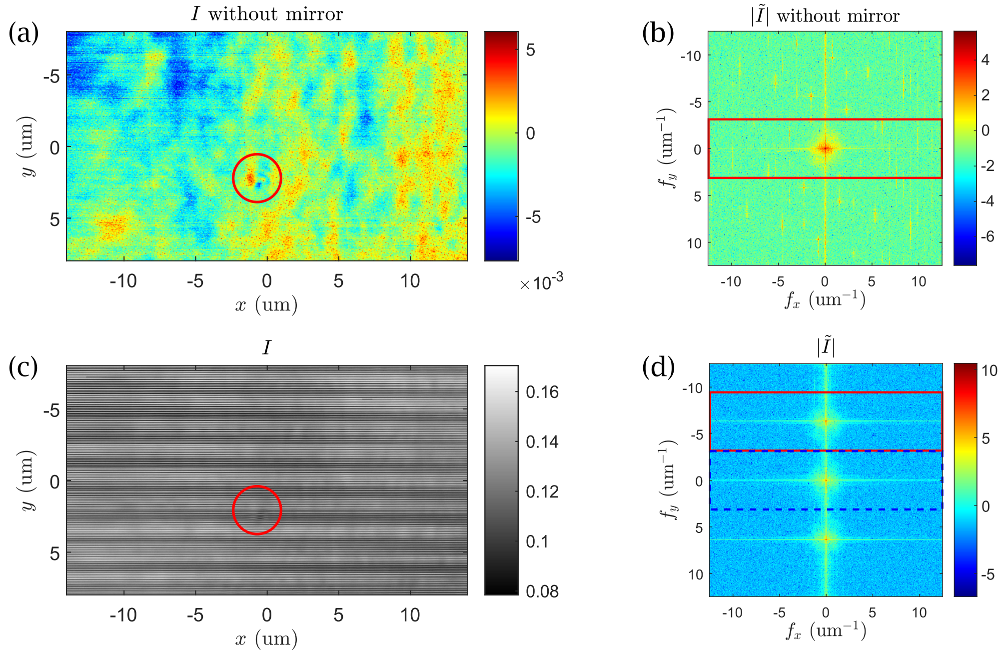

Figure 3.13: **(a)** Conventional CFS measurement of a 60 nm PSL particle and **(b)** its Fourier transform (logarithmic scale). **(c)** HCFS measurement of the same particle and its FT (logarithmic scale). Raster scan parameters: 700×400 pixels, 28×16 um^2, imaging time 80 seconds. In (a) and (c), the particle location is indicated by a red circle. In (b), the solid red window indicates where the filter is applied. In (d), the solid red window indicates the first order, and the dashed blue window indicates the zero order. The exact same band pass filter is used for each Fourier filtering step.

Again, using HCFS with $N = 4$ mirror stepping movement, i.e. every 4 lines the reference phase changes by 2π, we recorded the hologram I (Figure 3.13c). Following the standard Fourier reconstruction procedure with a band pass filter, the first and zero order reconstructions are shown in Figure 3.14 together with their SNR. Also, the unfiltered and filtered maps of the conventional CFS are included as a reference. We see both the real and imaginary part of the first order contains a signal that is similar to the conventional CFS signal, where two peaks with opposite signs are located adjacent to each other. From the simulation in section 3.2.1, we expect that real and imaginary signals to be flipped versions of each other, i.e. one signal is a "plus-minus" (first maximum and then minimum) and other is a "minus-plus". However, both signals are "minus-plus" in this case, we explain this by the extremely phase-sensitive nature of HCFS and unavoidable aberrations, such as tilt and defocus. On the other hand, the first order amplitude is fairly consistent with the simulation, as we can see two symmetrical peaks.

Regarding the signal-to-noise ratios, the imaginary part of the first order reconstruction (displayed in Figure 3.14b) achieves a SNR of approximately 10 dB, despite the size of the particle and the wavelength of our laser. Therefore, we expect that this setup is able to detect even smaller PSL particles. Compared to the reference, HCFS has a higher signal amplitude, a SNR gain of 7.5 dB is achieved over the unfiltered signal and a gain of 4 dB over the filtered signal. Dealing with low SNR measurements, a SNR increase of 4 dB is very meaningful, as it makes the particle much more distinguishable from the background.

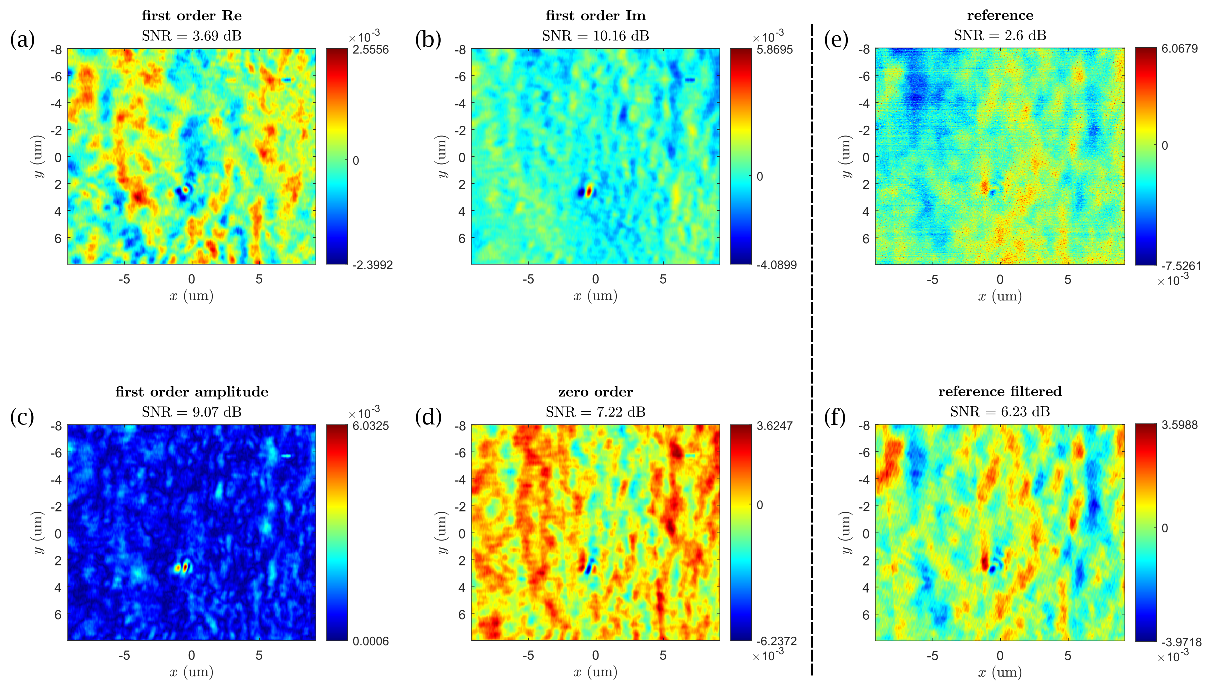

Figure 3.14: **(a)** The real component, **(b)** the imaginary component and **(c)** the amplitude of the first order reconstruction. **(d)** The zero order reconstruction. **(e)** Unfiltered signal of conventional CFS. **(f)** Filtered signal of conventional CFS with the same band pass filter. For each plot, 4.8 um of data are removed from both sides of x to eliminate the scanning artifact, then SNR are computed and shown.

Localization
Previously, localization of spherical particles was done by determining the zero-crossing position of the differential signal [30]. Here, we will briefly demonstrate an alternative method for particle localization using the phase information. As mentioned in section 3.2.1, the phase or more accurately the argument of the first order contains a discontinuity between the left and right sides of the particle. Assuming the particle is a perfect sphere, this discontinuity gives the x-coordinate of the particle location. To get the precise y-coordinate, we need additionally the top-bottom differential signal, for instance, by using a quadrant detector.

In Figure 3.15a, we show the argument of the first order reconstruction. As we expect, this information does not help us detect the particle, as the background contains mainly noise. However, we can identify the region where the particle is located using the differential signals. Subsequently, we can cut out this region as indicated by the red circle, additionally, the zoom into this region is shown in b. We can see that the left and right side have more or less constant arguments and there is about a π difference between them. Moreover, there is clearly a discontinuity in the center. By computing the finite difference in the x-direction (shown in c), we accentuate this discontinuity and the peak gives us the location of the particle. A cross section of the argument and its difference is displayed in Figure 3.15d. It seems like this method gives us pixel level precision of the particle location. However, the accuracy in this case should be in the order of 2-4 pixels (80-160 nm), as uncertainty of the argument grows if the amplitude gets closer to zero, and depends on the noise level. This explains the spikes around the discontinuity. Thus, higher SNR will translate to a higher level of accuracy of localization.

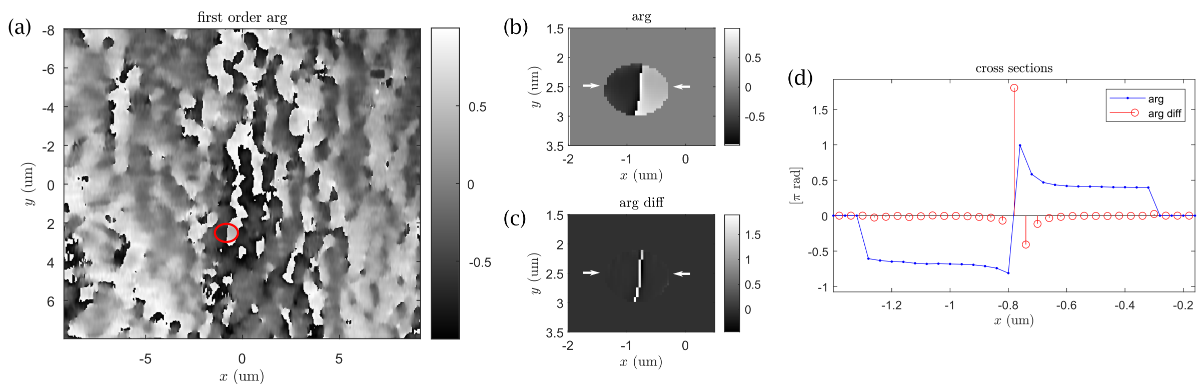

Figure 3.15: **(a)** The argument of the first order reconstruction. **(b)** Zoom of the particle region, indicated by the red circle. **(c)** Zoom of the particle region after computing the finite difference in the x-direction. **(d)** Cross sections in x as indicated by the white arrows in (b) and (c). All values are in units of π rad.

3.3. Discussions

In this chapter, we demonstrated the use of SOH in order to improve the sensitivity of CFS for detecting particles on a Si wafer. Using SNR as the performance metric, we saw consistently that HCFS is more sensitive than conventional CFS.

The SOH technique, commonly deployed for phase retrieval, allows us to retrieve the complex value differential signal C. But instead of utilizing the amplitude and phase information, in this thesis we mainly use the real and imaginary part of this complex signal. First of all, because the phase information does not help us distinguish the particle from the background. Another reason is that one out of the real and imaginary signals has a higher SNR than the amplitude, as we observed throughout this chapter. Amplitude, which is the incoherent sum of both parts, will therefore have a signal-to-noise ratio in the middle of the two. However, the real and imaginary part of C are subject to phase offsets, hence, it is inconsistent over different scans. Therefore, the amplitude of C is a more consistent benchmark.

One of the reasons we are able to achieve a higher SNR is due to the relatively strong reference field. Even though the field difference C (when $|U_\mathrm{R}| = 1$ normalized) should produce a lower amplitude than the intensity difference, as we demonstrated in section 3.2.1 with the simulation. Thanks to the high amplitude of the reference field, the first order term $|U_\mathrm{R}|C(x,y)e^{-i\phi_\mathrm{R}(x,y)}$ gets a boost in signal strength without using additional power. Considering the 30% reflectivity of silicon and slight optical losses from the objective, we estimate the average amplitude ratio between the reference and scattered field $\frac{|U_\mathrm{R}|}{|U_\mathrm{S}|}$ to be approximately 2.

Mirror movement

The HCFS results found in the chapter are all acquired using the stepping mirror movement we described, which is recently also used in [22, 34]. More specifically, the mirror positions are being cycled such that only the first $\lambda/2$ of piezo's range is used. Previously, linear ramp movement was generally used in synthetic optical holography [32, 33]. The main reason for us to choose stepping over the ramp has to do with our piezo's limited range of 15 um.

The main difference between the two movements is that stepping produces modulation only in the y-direction. However, with the linear movement the synthetic reference wave component k_x is typically 2-3 orders smaller than k_y, meaning that the modulation in x is scarce nonetheless. On the other hand, it is advantageous to use a smaller part of total piezo range, as the reference phase is more consistent throughout the whole scan. In fact, we see that the reference phase becomes more tilted as the reference mirror propagates with the linear movement, implying a tilt of the piezo mount.

Fourier reconstruction

The reconstruction process of HCFS is non-different from the standard digital off-axis holography. It involves isolating a particular order in the Fourier space with a window, typically a low pass filter e.g. Gaussian, Hamming or cosine, followed by shifting and inverse Fourier transforming.

We found in section 3.2.2 that the use of a band pass filter is needed to reconstruct the HCFS signal properly. This is because we need to get rid of the vertical frequencies that distort the background of the reconstruction. This "noise" comes mainly from the moving mirror and the background fluctuation, as discussed in Appendix A.7, and we can justify cutting out this part of the frequencies, because the expected particle signal doesn't occupy this part of the Fourier spectrum. Furthermore, there are horizontal frequency components at each order, e.g. in Figure 3.8c; they are also present in previous works of SOH [32, 33]. We suspect the cause to be instability of the raster scan, as this phenomenon is also present with the conventional CFS, and it is amplified by the interferometer. After reconstruction, this phenomenon results in big swings in amplitude near the left and right edges on the image, an example is displayed in Figure 3.16. For now, we deal with it by cropping the edges of the image, meaning that we lost some information. However, we can afford to scan a relatively large distance in the fast-scanning direction x without increasing too much the scanning time.

Other limitations

Although we are able to scan and reconstruct a relatively large area, the speed of the scans is limited by the required oversampling. Because SOH is a method that relies on spatial filtering, thus the zero and first orders need to be separate in the Fourier space. Therefore, some degree of oversampling is required in the slow-scanning direction y for smaller particles, which ultimately limits the imaging speed. In this case, we are able to detect the smallest particles with line separation (between two left-right lines) $2\Delta y = 0.04$ um.

One of the major performance limiting factors of the HCFS is the mechanical stability. Our setup is based

on a Michelson interferometer, where the object and reference beams interfere via separate paths. Thus, any mechanical vibration or air disturbance, even marginal, can cause different influences on the two separated interference beams [38]. Randomness in the optical path difference results in multiplicative noise proportional to the intensity [5]. Furthermore, alignment is a major limiting factor too. As the first order differential signal is phase dependent, any misalignment (e.g. defocus, tilt) will affect the signal. Because the sample is slightly tilted, the focal spot on the wafer can go in and out of focus during the raster scan. Moreover, we demonstrate in Appendix A.8 another tilt related issue with simulations, namely, a tilted reference beam. We see that a small tilt can cause unbalance and distortion of the first order signal. In contrast, the conventional CFS is much less sensitive to these two factors, so the measurements are more consistent and repeatable.

Ultimately, the resolution of HCFS is still limited by the surface roughness of the Si wafer, where the scattering cross section of the particle is in the order of the surface roughness [13]. We recall that CFS is not a resolution enhancement technique, but a sensitivity enhancement technique.

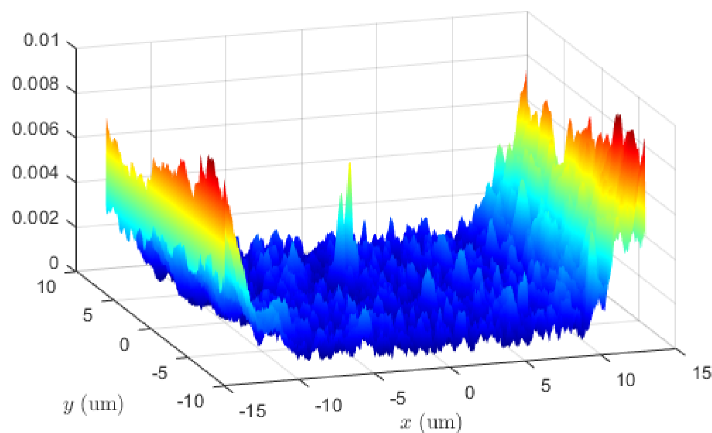

Figure 3.16: Surface plot of the amplitude shown in Figure 3.14c without removing the scanning artifact on both sides.

4

Conclusion and recommendations

4.1. Conclusion

In this thesis, we demonstrated the use of synthetic optical holography (SOH) as a new method to improve the sensitivity of coherent Fourier scatterometry (CFS) for particle detection. The implementation of SOH in the CFS is relatively simple, as only a 1D piezo stage with a mirror needs to be added. The hologram from this combined technique (HCFS) still contains the conventional CFS signal, which is the intensity difference between the two halves of the far field, as the zero order centered at the origin of the Fourier space. Furthermore, we derived that the first order modulated signal equals the complex far field difference scaled by the reference field amplitude. With simulation, we showed the real and imaginary parts of this signal are very similar to the conventional differential signal.

Overall, we could see consistent signal-to-noise ratio (SNR) improvement over the conventional CFS, as the reference field boosts the signal strength. We demonstrated with measurements of a dust particle using a very low amount of incident power (0.0014 mW) a SNR gain of more than 6 dB compared to filtered CFS signal. It is thanks to the attenuation of low frequency electronic noises, similar to the heterodyne detection [11]. For the detection of a PSL particle with diameter of 60 nm ($\sim \lambda/10$) on Si wafer, this new implementation leads to a SNR of 10 dB, which is about 4 dB over the filtered conventional CFS signal. We envision that HCFS is able to detect even smaller particles with the current wavelength of 633 nm.

However, this implementation is more prone to mechanical instabilities and alignment tolerances. As a result, the measurements are less consistent and some artifacts arise. We dealt with these artifacts by using a non-trivial band pass filter and removing distorted edge data during the reconstruction process. Thus, further investigation and research are needed to optimize this technique.

4.2. Recommendations

First, we would present an idea of a "dark-field" cross polarization CFS. In typical dark-field particle detection techniques, specular reflections are blocked, so only scattered light is captured by the detectors. We propose a similar approach for CFS utilizing polarization states. The idea is that when linearly polarized light is focused on a flat surface, the specularly reflected light will have the same polarization as the incidence. If we block this polarization using a polarizer in the orthogonal direction, only the change of polarization due to the presence of a scatterer is captured by the detector. Typically, the signal of a dark-field technique is very weak, thus a lot of illumination power is required. However, we envision that HCFS can boost the signal strength a lot with the reference beam. The implementation will probably look like that in Figure 4.2. The incident light is a s-polarized beam. In front of the detector a polarizer is installed to capture only the p-polarization component of the scattered far field. The reference beam is converted to p-polarization by passing through a Faraday rotator twice, for interfering with the dark-field.

Next, we would like to suggest a few ways to further improve the sensitivity of the current system. We showed in equation 2.8 that the first order signal of HCFS is a product of $|U_\mathrm{R}|$ and C (complex field difference). So, to enhance sensitivity, we would aim to increase one of these two terms.

It is demonstrated that the use of radially polarized light improves the sensitivity of CFS [30]. Thus, we suggest a theoretical study for using radially polarized light in HCFS. The x and y components of radial polarization have a π phase difference between the two halves of the beam. In Figure 4.1, the x-component is shown. One can investigate the use of a radially polarized sample beam and a linearly polarized reference beam. We imagine that the first order signal, which is phase dependent, will be drastically different from now.

In theory, we can boost this first order signal further by increasing the strength of the reference beam without extra incident power on the wafer, similar to optical heterodyne detection [23]. This could be beneficial for biological applications or inspection of plastic substrates, where too much power would mean damage to either the substrate or the specimen [11]. However, increasing the intensity will also increase the noise caused by mechanical instabilities. We suggest to investigate the optimal ratio of $\frac{|U_\mathrm{R}|}{|U_\mathrm{S}|}$, where the sensitivity enhancement is maximum.

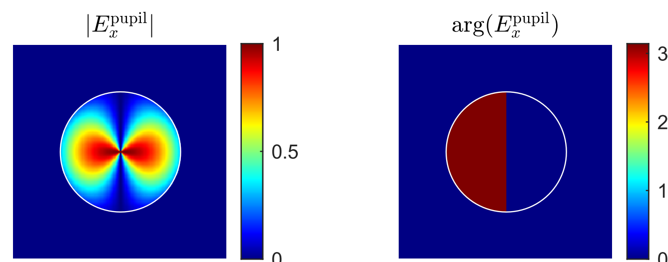

Figure 4.1: The x-component for a radially polarized beam at the pupil plane. The normalized amplitude is shown on the left and the phase on the right.

In order to implement some of the above mentioned ideas, the setup needs to be adjusted. As the current setup does not allow us to increase the reference beam intensity nor to apply different polarization to the sample and reference beam. A possible configuration has already been suggested for the interferometric CFS [27], where an extra beam splitter is placed before BS1 to split the incident beam into a sample beam and a reference beam. Instead of a flat reference mirror, a retro-reflector is attached to the moving piezo stage. The intensity of the two beams is controlled by the split ratio of this extra beam splitter and the polarization states can be controlled individually.

We suggest hereby another configuration that is closer to the current one, it is displayed in Figure 4.3. The incident beam is split accordingly at the source, subsequently, the reference and sample beams are coupled individually to the main setup, thus the polarization states can be separately controlled with polarizers P1 and P2. However, this configuration acquires a lot more extra space, decreasing the compactness of the original CFS. Also, it is also more subject to misalignment and instability, as the two beams have mostly separate paths and the number of optical components is increased.

Beyond the detection of contamination on wafers, HCFS could also be employed when the contrast between the nanoparticles and substrate is low, such as PSL particle on glass or pellicle. Due to the phase sensitive nature, HCFS could be much more sensitive than conventional CFS.

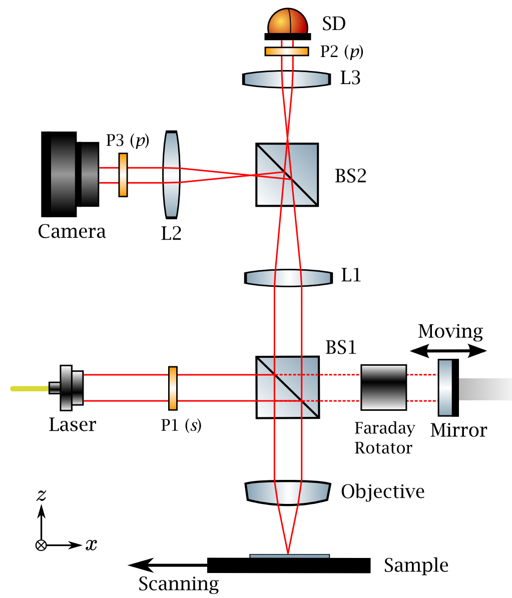

Figure 4.2: A possible dark-field HCFS configuration. The incident beam is s-polarized by P1. The Faraday rotator in the reference arm converts s-polarization into p. At the detector, polarizer pair P2-P3 allows us to select the p-polarization component of the far field.

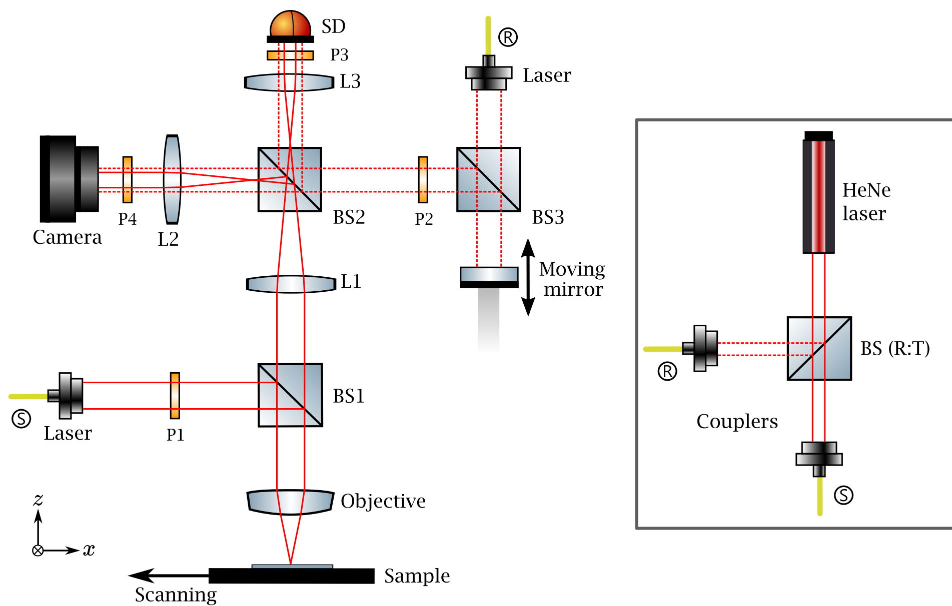

Figure 4.3: A possible HCFS configuration. The laser beam is split with a beam splitter with the desired split ratio (R:T) before being coupled individually to the main setup. Polarizer pair P1-P2 allows us to select the polarization state of the two beams independent of each other, and P3-P4 lets us select the field component (x or y) at the detector.

Acknowledgement

I would like to express my gratitude to my supervisors Silvania Pereira and Dmytro Kolenov. Their continuous guidance and advice helped me through all stages of this project. Dmytro spent a lot of time helping me with the lab work and provided me with the simulation data I used in this thesis, which I have truly appreciated. Also, I would like to thank Roland Horsten and Thim Zuidwijk for their support, without their expertise I would not be able to achieve the final results.

License

Schematics of optical setups in this thesis are created using the (modified) optical components from ComponentLibrary. ComponentLibrary by Alexander Franzen is licensed under a Creative Commons Attribution-NonCommercial 3.0 Unported License.
The front cover photo is by toms from FreeImages [35].

A

Appendix

A.1. Fourier transform

In this thesis, we use the following general definition of 2D Fourier transform (FT) and inverse Fourier transform (IFT).

$$\begin{aligned}\mathscr{F}\left\{g(x,y)\right\} &= \iint g(x,y)e^{-i2\pi(f_x x+f_y y)}dxdy \\ \mathscr{F}^{-1}\left\{G(f_x,f_y)\right\} &= \iint G(f_x,f_y)e^{i2\pi(f_x x+f_y y)}df_x df_y\end{aligned} \tag{A.1}$$

However, we deal with sampled intensity images in digital holography, thus fast Fourier transform (FFT) is used instead. The 2D Fourier transform Y of a m-by-n matrix X is given by:

$$Y_{p+1,q+1} = \sum_{j=0}^{m-1}\sum_{k=0}^{n-1} e^{-i2\pi jp/m}e^{-i2\pi kq/n}X_{j+1,k+1} \tag{A.2}$$

, p and j are indices that run from 0 to m–1, and q and k are indices that run from 0 to n–1.

Some useful Fourier properties are listed below [7].

1. **Modulation property.** If $\mathscr{F}\{g(x,y)\} = G(f_x,f_y)$ then

$$\mathscr{F}\left\{g(x,y)e^{i2\pi(ax+by)}\right\} = G\left(f_x-a,f_y-b\right). \tag{A.3}$$

2. **Convolution property.** If $\mathscr{F}\{g(x,y)\} = G(f_x,f_y)$ and $\mathscr{F}\{h(x,y)\} = H(f_x,f_y)$ then

$$\mathscr{F}\left\{g(x,y)\otimes h(x,y)\right\} = G\left(f_x,f_y\right)H\left(f_x,f_y\right) \tag{A.4}$$

and

$$\mathscr{F}\left\{g(x,y)h(x,y)\right\} = G\left(f_x,f_y\right)\otimes H\left(f_x,f_y\right), \tag{A.5}$$

where $\otimes$ denotes the operation of convolution.

A.2. Derivation of SOH signal

In this Appendix, we derive the equation of the hologram obtained from SOH phase imaging technique. The voltage of the photo-detector is proportional to the total intensity of the interference pattern between the scattered and the reference beam.

$$V(x,y) \propto I = \iint \left| U_{\mathrm{R}}(x,y,\xi,\eta) + U_{\mathrm{S}}(x,y,\xi,\eta) \right|^2 \; d\xi d\eta \tag{A.6}$$

The absolute square can be written as a product of complex conjugates and the whole expression can be worked out further.

$$\begin{aligned} &= \iint \{U_{\mathrm{R}} + U_{\mathrm{S}}\}\{U_{\mathrm{R}} + U_{\mathrm{S}}\}^* \, d\xi d\eta \\ &= \iint \left(|U_{\mathrm{R}}|^2 + |U_{\mathrm{S}}|^2 + U_{\mathrm{R}}^* U_{\mathrm{S}} + U_{\mathrm{R}} U_{\mathrm{S}}^*\right) d\xi d\eta \end{aligned} \tag{A.7}$$

If we assume that U_{R} and U_{S} are uniform on the detector plane (both amplitude and phase), we can drop the integration and obtain the following expression.

$$\propto |U_{\mathrm{R}}(x,y)|^2 + |U_{\mathrm{S}}(x,y)|^2 + U_{\mathrm{R}}^*(x,y) U_{\mathrm{S}}(x,y) + U_{\mathrm{R}}(x,y) U_{\mathrm{S}}^*(x,y) \tag{A.8}$$

But in practice, these two beams are often the center part of a large Gaussian beam, so the amplitudes will vary slightly. Also, the reflected field U_{S} is generally not constant in phase, as it contains defocus of a certain degree and aberrations from the objective.

A.3. Derivation of differential signal

We start by writing the differential signal as the integrated intensity difference between the interference pattern on both sides of the detector. For convenience, we may drop the notation of sample spatial coordinates (x, y), because virtually every quantity has this dependency.

$$V(x,y) \propto I_1 - I_2 = \iint_{D_1} \left|U_R + U_S(\xi_1,\eta_1)\right|^2 d\xi_1 d\eta_1 - \iint_{D_2} \left|U_R + U_S(\xi_2,\eta_2)\right|^2 d\xi_2 d\eta_2 \tag{A.9}$$

We can expand the square modulus terms.

$$\begin{aligned} &= \iint_{D_1} \left(|U_R|^2 + |U_S(\xi_1,\eta_1)|^2 + U_R^* U_S(\xi_1,\eta_1) + U_R U_S^*(\xi_1,\eta_1)\right) d\xi_1 d\eta_1 \\ &- \iint_{D_2} \left(|U_R|^2 + |U_S(\xi_2,\eta_2)|^2 + U_R^* U_S(\xi_2,\eta_2) + U_R U_S^*(\xi_2,\eta_2)\right) d\xi_2 d\eta_2 \end{aligned} \tag{A.10}$$

We assume U_R to be uniform across the entire detector (both amplitude and phase), so the first terms of the two integrals cancel each other out. Also, we can separate the two terms with $|U_S|^2$, and replace them with $I_{\text{diff,no mirror}}$ from eq 2.1, yielding

$$= I_{\text{diff,no mirror}} + \iint_{D_1} \left(U_R^* U_S(\xi_1,\eta_1) + U_R U_S^*(\xi_1,\eta_1)\right) d\xi_1 d\eta_1 - \iint_{D_2} \left(U_R^* U_S(\xi_2,\eta_2) + U_R U_S^*(\xi_2,\eta_2)\right) d\xi_2 d\eta_2. \tag{A.11}$$

Next, we take out U_R from the integrals and rearrange the terms.

$$\begin{aligned} =& I_{\text{diff,no mirror}} + U_R \left\{ \iint_{D_1} U_S^*(\xi_1,\eta_1) d\xi_1 d\eta_1 - \iint_{D_2} U_S^*(\xi_2,\eta_2) d\xi_2 d\eta_2 \right\} \\ &+ U_R^* \left\{ \iint_{D_1} U_S(\xi_1,\eta_1) d\xi_1 d\eta_1 - \iint_{D_2} U_S(\xi_2,\eta_2) d\xi_2 d\eta_2 \right\} \end{aligned} \tag{A.12}$$

We see that the two terms in accolades are complex conjugates with each other, so we replace them with $C(x, y)$.

$$= I_{\text{diff,no mirror}} + U_R C^*(x,y) + U_R^* C(x,y) \tag{A.13}$$

Lastly, we write the reference field $U_R(x, y)$ as $|U_R|e^{i\phi_R(x,y)}$, ending up in a formula containing three orders.

$$= I_{\text{diff,no mirror}} + |U_R| C^*(x,y) e^{i\phi_R(x,y)} + |U_R| C(x,y) e^{-i\phi_R(x,y)} \tag{A.14}$$

The complex term $C(x, y)$ equals the integrated complex field difference between both sides of the detector at each position.

$$\iint_{D_1} U_S(\xi_1,\eta_1) d\xi_1 d\eta_1 - \iint_{D_2} U_S(\xi_2,\eta_2) d\xi_2 d\eta_2 \tag{A.15}$$

The Fourier transform of the intensity (A.14) is

$$\tilde{I}_{\text{diff,no mirror}}(\mathbf{q}) + |U_R| \tilde{C}^* \left(\mathbf{q} - \mathbf{k}_\parallel\right) + |U_R| \tilde{C} \left(\mathbf{q} + \mathbf{k}_\parallel\right), \tag{A.16}$$

where $\tilde{I}_{\text{diff,no mirror}}$ the Fourier transform of $I_{\text{diff,no mirror}}$, which corresponds to the differential signal without interferometer, and $\tilde{C}$ the Fourier transform of $C(x, y)$.

A.4. LabVIEW measurement program

We have added the mirror movements of SOH from section 2.2 to the existing LabVIEW scanning program, so every parameter related to a HCFS measurement can be controlled from this program. In Figure A.1, the front panel of the LabVIEW program is shown. The red window indicates the additional controls for the reference mirror, and the rest of the program is the existing part. Both the linear movement and the stepping are implemented, where one can toggle between using the switch on the left. Currently, these movements are programmed with for-loops, but ideally it should be done with wave forms. However, the stepping option works very well, as the synchronization with the raster scan is good and it doesn't have range issues thanks to position resetting. Hence, we mainly use this option in this thesis. The two important parameters are "wavelength" λ and "# steps" N, the positions of the mirror are then calculated automatically.

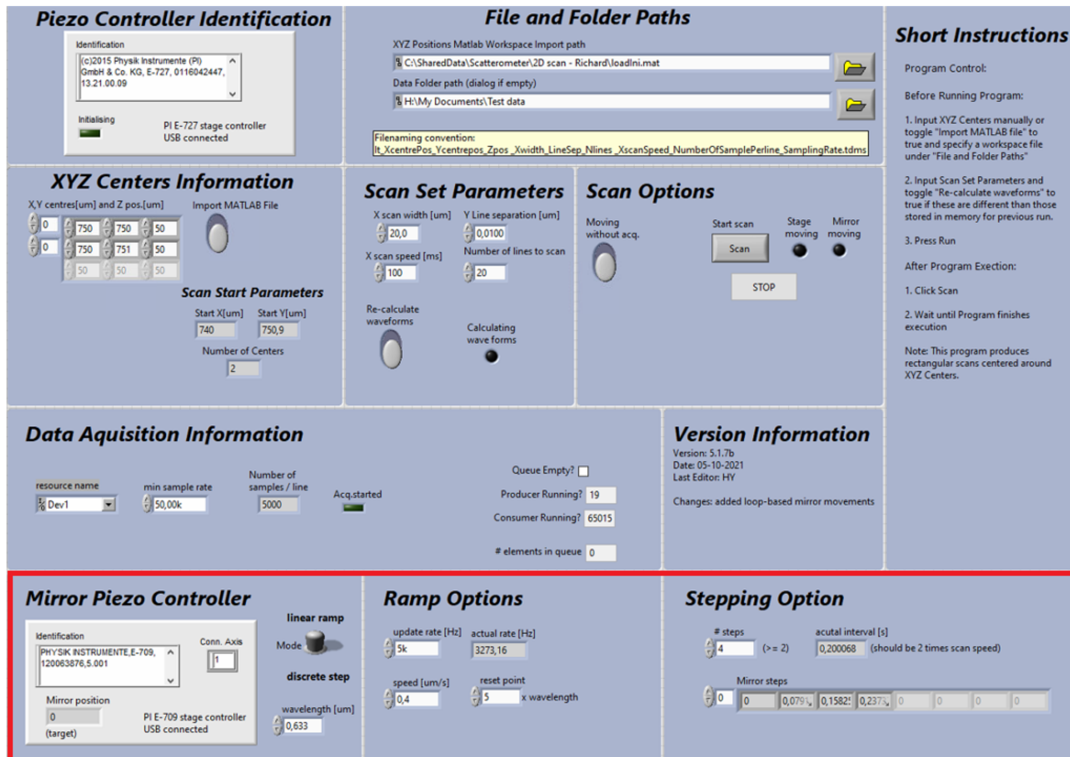

Figure A.1: The LabVIEW program for our measurements with newly implemented mirror controls indicated by the red window.

A.5. Sample tilt

As mentioned in section 3.1, where we are using the SOH technique to retrieve the height of the letter 'P' structure , we have noticed a small tilt of the sample while scanning. An effort has been made to get rid of this tilt in order to improve the quality of scan.

First, we look at the tilt in the x-direction with the manual control. With the beam focused on a flat area of the wafer, we adjust and fix the (silicon) reference mirror such that vertical fringes are visible on the camera, these fringes help us to see the change of phase or height. An example is displayed in Figure A.2, the setup is essentially a Michelson interferometer if the height of the sample changes, we will observe a shift of the fringes. By turning a knob on the x-axis, the whole stage and sample are moved, the amount of displacement is measured with a digital profile gauge. Initially, a distance of about 140 um is measured that takes to change the phase by 2π, corresponding to a height change of $\lambda/2$ or a tilt of 0.13°. The base of the stack has a length of 14 cm, so we need to raise one side of the base by 320 um to compensate for the tilt, which is done by placing 4 pieces of paper under the stack. Repeating the previous steps, we see that the tilt is mostly gone. Next, when we perform a raster scan with the stage, however, we observe again the same amount of tilt in the x-direction as before the compensation. So this method of minimizing the tilt seems not to be affecting the actual scan.

The same findings are seen on the y-axis, also for a different smaller xy-stage (PI P622.2). We are yet not able to understand the cause of this phenomenon, so a more thorough and systematic investigation of the setup is needed.

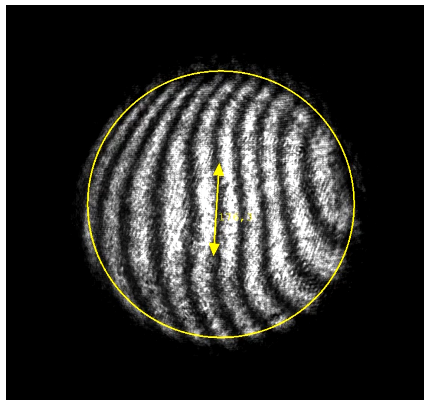

Figure A.2: The interference pattern that is used to determine the tilt of the sample. A silicon mirror with a pinhole is installed here. The vertical arrow is for identifying a single fringe. When the phase of the scattered field changes, we see a horizontal shift in the interference pattern.

A.6. Through-focus scans

In section 3.2.2, we demonstrate a new method for quick focusing by minimizing the interference fringes between the reflected and the reference beam. In order to determine how well the focus is using this method, we use the so-called through-focus procedure [12]. First, we estimate the optimal focal position by looking at the interference pattern. This position will be our zero point of reference. Next, we scan a known particle or structure on the wafer multiple times while varying the z-position with a vertical stage with the conventional CFS. In our case, a round Si structure of 518 nm in diameter with a height of 150 nm is scanned, and the change in height Δz ranges from -1 to 1 um in steps of 0.1 um, plus two extra steps of 0.05 um near zero. Signals of some of the positions are plotted in Figure A.4. The largest peak-to-peak amplitude and the smallest imbalance of the signal tell us the optimal focal position.

In Figure A.3, the peak-to-peak and the S-curve (imbalance) is plotted against Δz. Note that Δz is defined as the z-stage's change in height, so larger Δz means smaller distance between objective and sample. From these graphs, we conclude that the position with $\Delta z = -0.1$ um is the optimal focus, where the peak-to-peak value is maximal and the signal imbalance is small. So with an accuracy of about 100 nm, we can say that focusing by means of the interference pattern is a fast and accurate method.

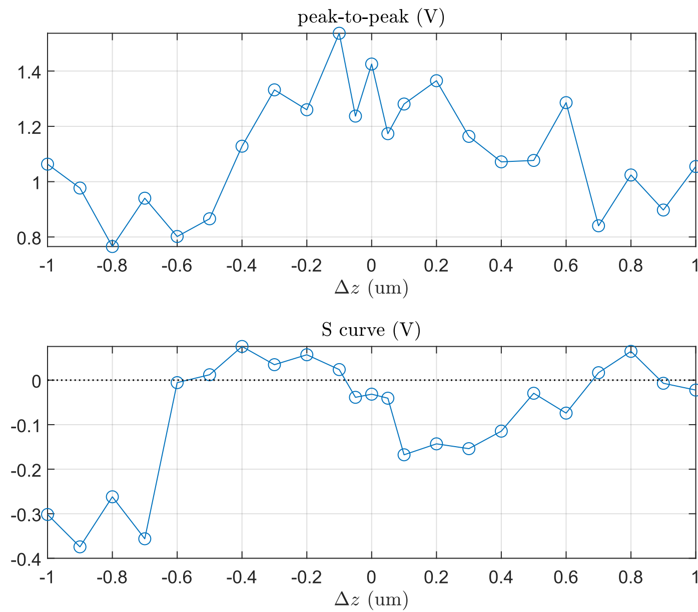

Figure A.3: Top: peak-to-peak amplitude of the signal against through-focus positions. Bottom: imbalance of the signal against through-focus positions.

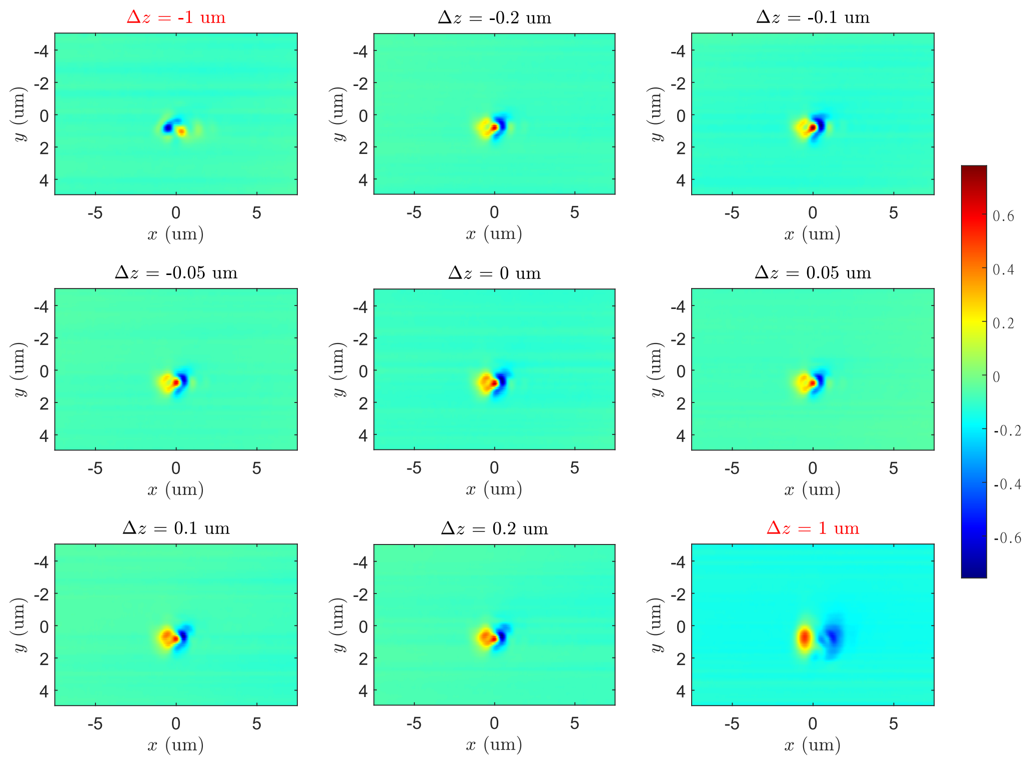

Figure A.4: CFS signals for the 7 center through-focus positions, also the two most extreme positions are included. The color scale is consistent through all graphs.

A.7. Background noise from reference mirror

In order to design an optimal filter to retrieve the particle signal, we look at the background noise spectrum from the stepping movement of the reference mirror. With the laser beam focused on the surface of a Si wafer, we start a measurement with $N = 4$, i.e. every 4 lines the reference phase changes with 2π. However, the sample stage is now stationary instead of performing a raster scan. Therefore, the entire measured signal is essentially noise from the imperfections and instabilities of the reference mirror.

In Figure A.5, we show the differential signal measured and its Fourier transform. A metallic mirror is used without a pinhole. The ideal signal is an uniform zero-valued image, however, we can see horizontal fringes where the maxima repeat every 4 lines. This is mainly caused by aberrations, as the reflected field contains aberrations from the objective. These aberrations are not necessarily symmetrical, thus the phase differences cause a non-zero differential signal when a reference beam is used. Furthermore, we can see small fluctuations within each line, caused by vibrations of the setup.

Looking at the Fourier transform, it is quite notable that the spectrum contains mainly frequencies in the y-direction and 0 in the x-direction. Coincidentally, the Fourier spectrum of a particle signal contains mainly non-zero x-frequencies, shown in Figure 3.5 from the simulation. Meaning that we can possibly remove this error without sacrificing the signal of the particle too much by cutting out the low spatial frequencies in the x-direction.

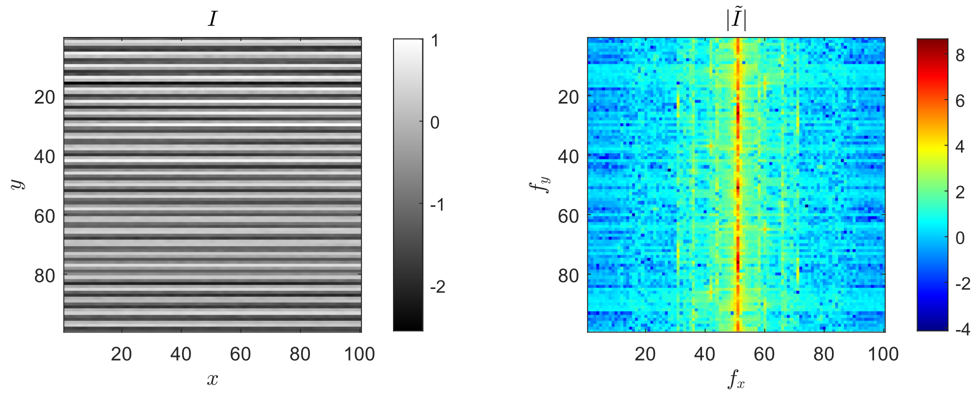

Figure A.5: Left: the measured differential signal with $N = 4$ stepping mirror and fixed sample. Right: amplitude of the Fourier transform (log scale). Units of the x and y axis are pixels.

A.8. Simulation - effect of tilt

Due to tolerance in alignments, an unavoidable source of error is the relative tilt between the reference field and the scattered field. This is unrelated to the sample tilt we investigated in Appendix A.5. In this Appendix, we look at how the signals are affected by the tilt modeled as an aberration with simulation.

We introduce a small tilt in the x-direction, the axis along which the signal is differentiated. The Zernike polynomial Z_1^1 corresponding to this tilt is shown in Figure A.6a. Applying this aberration to the scattered far field, we then simulate the HCFS signal, which we display in b. It looks very similar to the signal without aberration. However, we can see a significant change of the first order spectrum from the FT (c), it is no longer symmetrical. Zero order signal is unaffected, because of its independence of phase. By reconstructing the first order, we see the real part (e) is distorted, the imaginary part (f) as well as the amplitude (d) becomes unbalanced. Thus, we can say that the HCFS technique is extremely sensitive to aberrations due to phase dependency. On the other hand, a benefit of HCFS is the fact we still have the conventional differential signal as the zero order, which we can always fall back to.

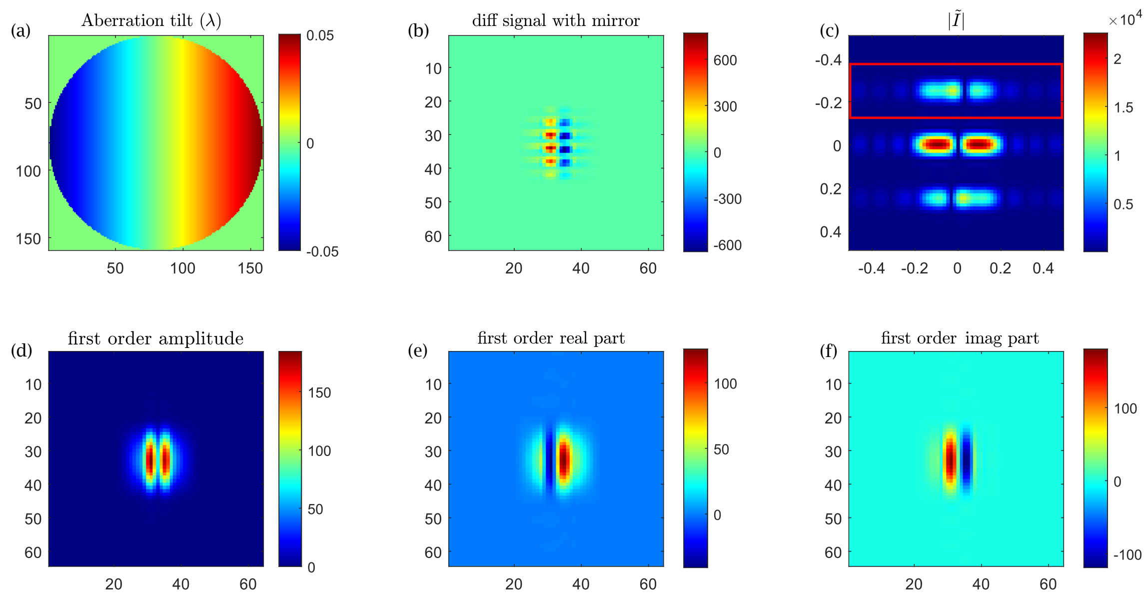

Figure A.6: **(a)** The tilt applied to the scatter far field, corresponding to Zernike polynomial Z_1^1. **(b)** Simulated HCFS signal with tilt aberration. **(c)** Amplitude of the Fourier transform of the HCFS signal. **(d)** Amplitude of the first order reconstruction using a rectangular window indicated by the red solid rectangle in (c), followed by **(e)** the real part and **(f)** the imaginary part.

A.9. Extra supporting results

Dust particle

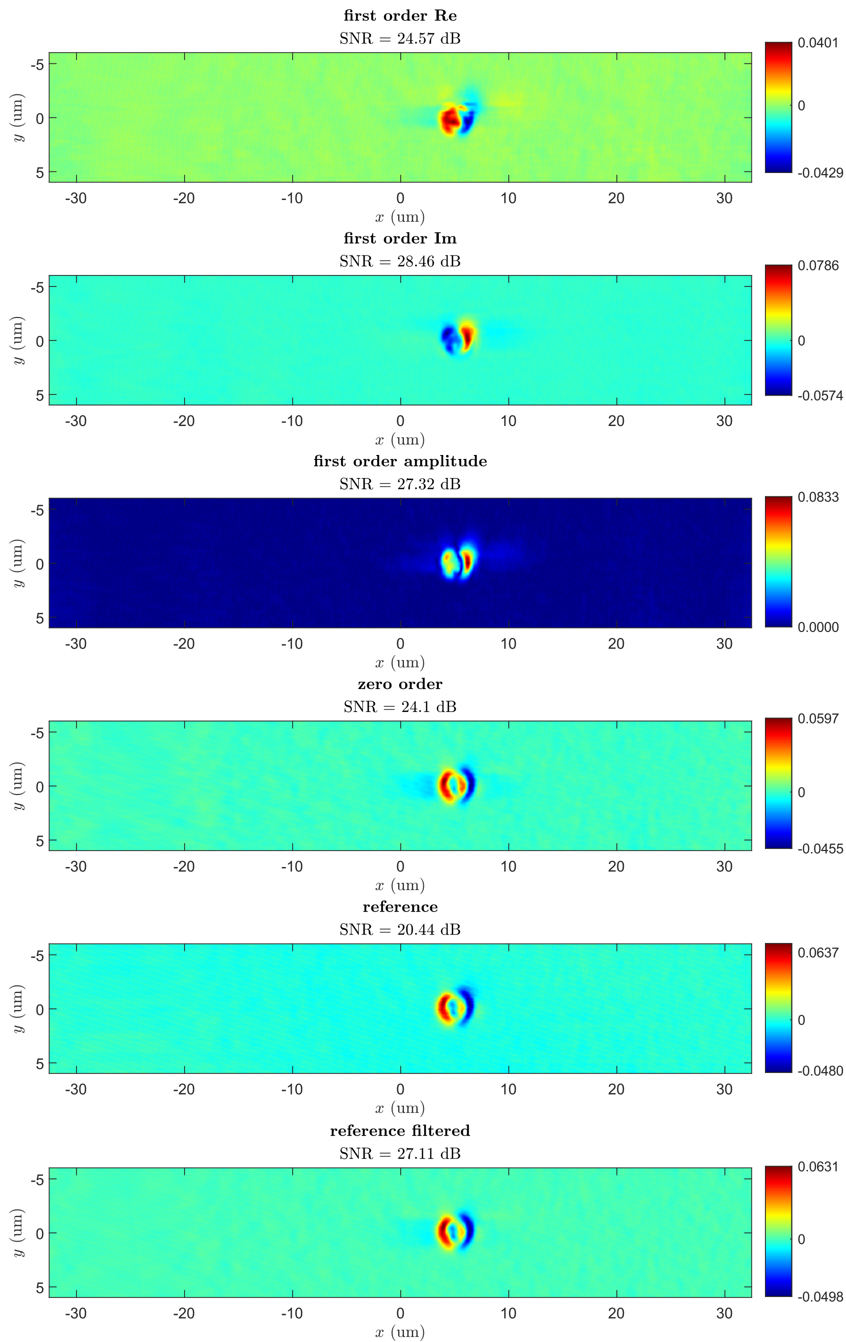

Figure A.7: Results of HCFS and conventional CFS (reference), corresponding to scan #2 in section 3.2.2.

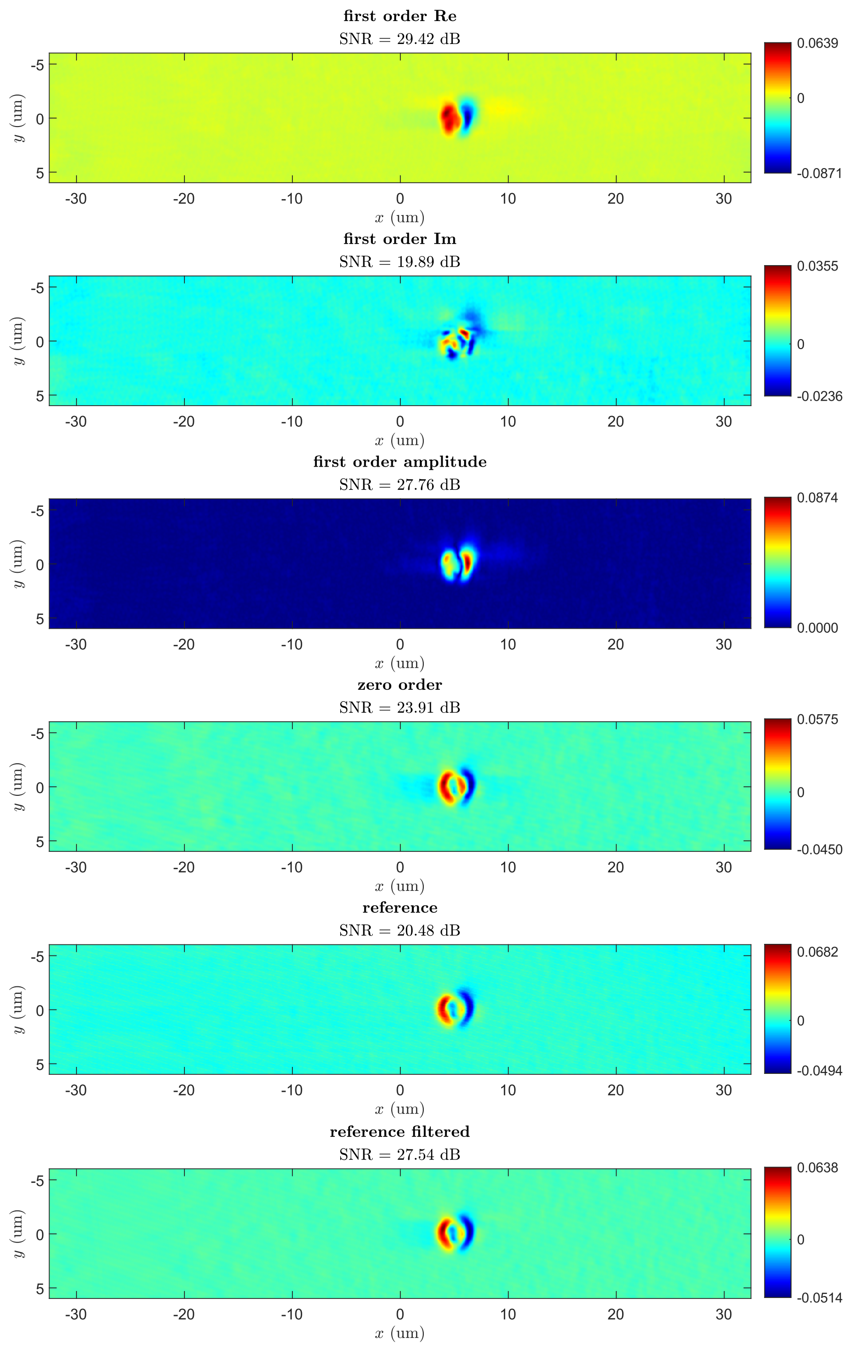

Figure A.8: Results of HCFS and conventional CFS (reference), corresponding to scan #3 in section 3.2.2.

Low power detection

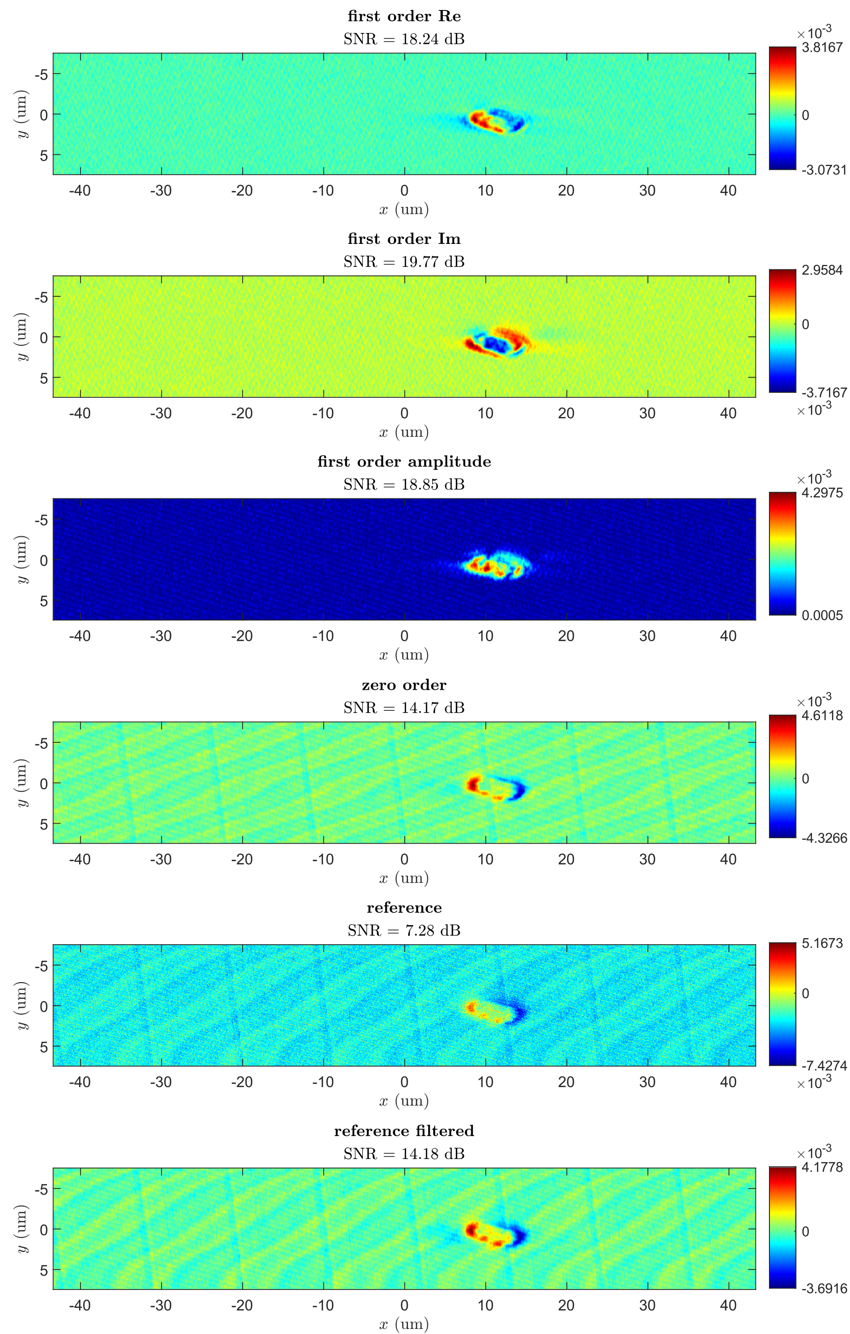

Figure A.9: Results of HCFS and conventional CFS (reference), corresponding to scan #2 in section 3.2.3.

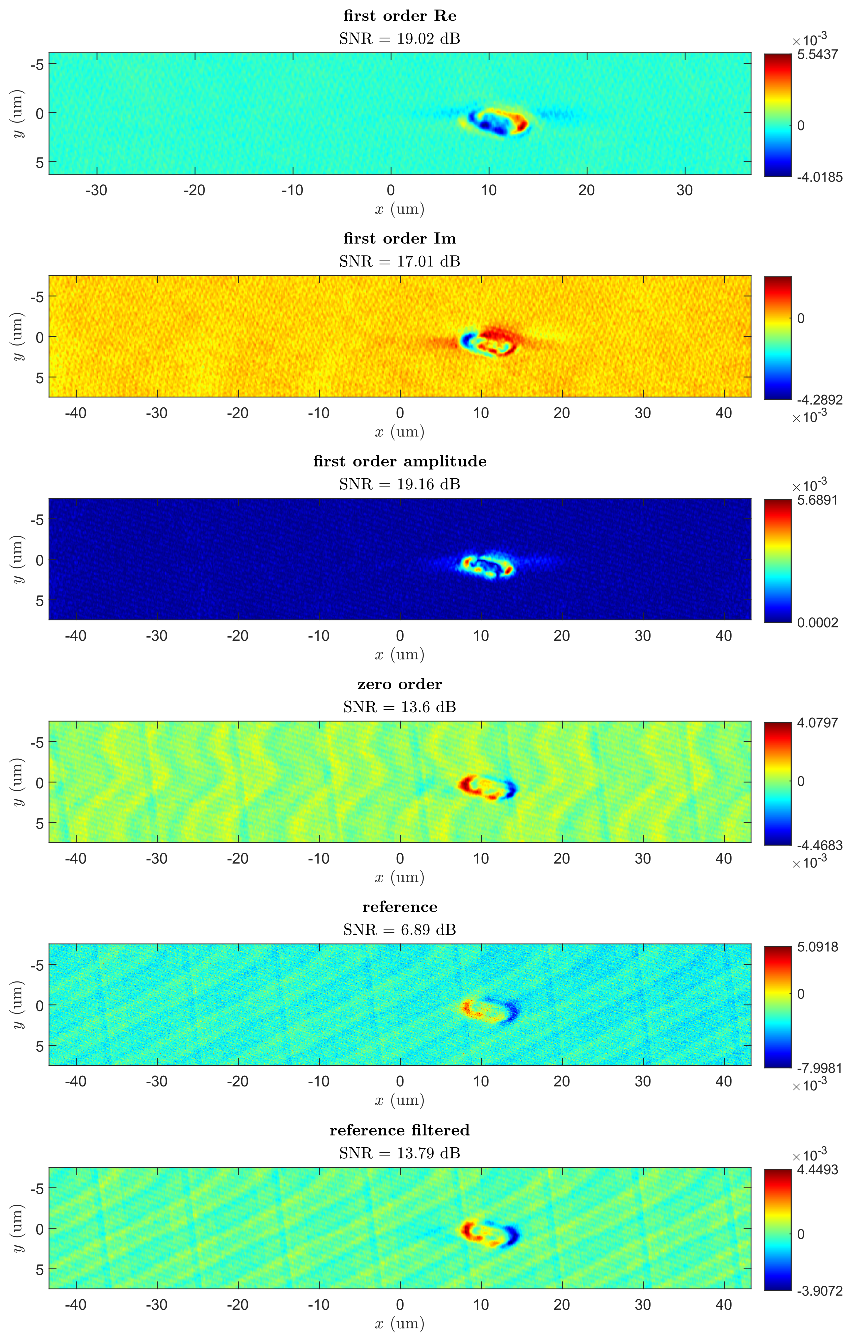

Figure A.10: Results of HCFS and conventional CFS (reference), corresponding to scan #3 in section 3.2.3.

Bibliography

[1] A. Chen, V. Huang, S. Chen, C.J. Tsai, K. Wu, H. Zhang, K. Sun, J. Saito, H. Chen, D. Hu, et al. Advanced inspection methodologies for detection and classification of killer substrate defects. *Lithography Asia 2008*, 7140:71400W, 2008.

[2] J. Cook. The zernike polynomials. *Journal of Modern Optics*, 23(8):679–680, 1976.

[3] A.J. Cox, A.J. DeWeerd, and J. Linden. An experiment to measure mie and rayleigh total scattering cross sections. *American Journal of Physics*, 70(6):620–625, 2002.

[4] E. Cuche, P. Marquet, and C. Depeursinge. Spatial filtering for zero-order and twin-image elimination in digital off-axis holography. *Applied optics*, 39(23):4070–4075, 2000.

[5] B. Deutsch, M. Schnell, R. Hillenbrand, and P. Scott Carney. Synthetic optical holography with nonlinear-phase reference. *Optics Express*, 22(22):26621–26634, 2014.

[6] O. El Gawhary, N. Kumar, S.F. Pereira, W.M.J. Coene, and H.P. Urbach. Performance analysis of coherent optical scatterometry. *Applied Physics B*, 105(4):775–781, 2011.

[7] R.M. Gray and J.W. Goodman. *Fourier transforms: an introduction for engineers*, volume 322. Springer Science & Business Media, 2012.

[8] A. Herráez, D.R. Burton, M.J. Lalor, and M.A. Gdeisat. Fast two-dimensional phase-unwrapping algorithm based on sorting by reliability following a noncontinuous path. *Applied optics*, 41(35):7437–7444, 2002.

[9] B. Jean-Luc and D. Bruno. Contamination monitoring and analysis in semiconductor manufacturing. *Semicond. Technol*, pages 57–78, 1999.

[10] M.F. Kasim. Fast 2d phase unwrapping implementation in matlab. `https://github.com/mfkasim91/unwrap_phase/`, 2017. Accessed: 5 November 2021.

[11] D. Kolenov, R.C. Horsten, and S.F. Pereira. Heterodyne detection system for nanoparticle detection using coherent fourier scatterometry. *Optical Measurement Systems for Industrial Inspection XI*, 11056: 110561A, 2019.

[12] D. Kolenov, P. Meng, and S. Pereira. A highly sensitive laser focus positioning method with submicrometre accuracy using coherent fourier scatterometry. *Measurement Science and Technology*, 31 (6):064007, 2020.

[13] D. Kolenov, I.E. Zadeh, R.C. Horsten, and S.F. Pereira. Direct detection of polystyrene equivalent nanoparticles with a diameter of 21 nm ($\lambda/19$) using coherent fourier scatterometry. *Optics Express*, 29(11):16487–16505, 2021.

[14] N. Kumar, O. El Gawhary, S. Roy, V.G. Kutchoukov, S.F. Pereira, W. Coene, and H.P. Urbach. Coherent fourier scatterometry: tool for improved sensitivity in semiconductor metrology. *Metrology, Inspection, and Process Control for Microlithography XXVI*, 8324:83240Q, 2012.

[15] N. Kumar, P. Petrik, G.K.P. Ramanandan, O. El Gawhary, S. Roy, S.F. Pereira, W.M.J. Coene, and H.P. Urbach. Reconstruction of sub-wavelength features and nano-positioning of gratings using coherent fourier scatterometry. *Optics express*, 22(20):24678–24688, 2014.

[16] N. Kumar, L. Cisotto, S. Roy, G.K.P. Ramanandan, S.F. Pereira, and H.P. Urbach. Determination of the full scattering matrix using coherent fourier scatterometry. *Applied optics*, 55(16):4408–4413, 2016.

[17] FDTD Lumerical. Solutions, 2016.

[18] C. Mack. *Fundamental principles of optical lithography: the science of microfabrication*, pages 105–106. John Wiley & Sons, 2008.

[19] A.A. Michelson and E.W. Morley. On the relative motion of the earth and of the luminiferous ether. *Sidereal Messenger*, 6:306–310, 1887.

[20] D. Monroe. Chips for artificial intelligence. *Communications of the ACM*, 61(4):15–17, 2018.

[21] G. Moona, P. Kapruwan, R. Sharma, and V.N. Ojha. Silicon wafer surface reflectance investigations by using different surface texturing parameters. *Proceedings of the National Academy of Sciences, India Section A: Physical Sciences*, 88(4):617–623, 2018.

[22] K. Neutsch, E.L. Gurevich, M.R. Hofmann, and N.C. Gerhardt. Investigation of laser-induced periodic surface structures using synthetic optical holography. *Nanomaterials*, 12(3):505, 2022.

[23] K. Nosu. Advanced coherent lightwave technologies. *IEEE Communications Magazine*, 26(2):15–21, 1988.

[24] J. Pawley. Handbook of biological confocal microscopy. 236:pages 9–12, 2006.

[25] T. Poon and J. Liu. *Introduction to modern digital holography: with MATLAB*. Cambridge University Press, 2014.

[26] J. Pospıšil and S. Nešpurek. Photostabilization of coatings. mechanisms and performance. *Progress in Polymer Science*, 25(9):1261–1335, 2000.

[27] S. Roy. *Sub-wavelength metrology using Coherent Fourier Scatterometry*. PhD thesis, Delft University of Technology, pages 110–111, 2016.

[28] S. Roy, N. Kumar, S.F. Pereira, and H.P. Urbach. Lowering the cross correlation between different shape parameters of the inverse grating problem in coherent fourier scatterometry. In *Fringe 2013*, pages 43–48. Springer, 2014.

[29] S. Roy, M. Bouwens, L. Wei, S.F. Pereira, H.P. Urbach, and P. Van Der Walle. High speed low power optical detection of sub-wavelength scatterer. *Review of Scientific Instruments*, 86(12):123111, 2015.

[30] S. Roy, K. Ushakova, Q. Van den Berg, S.F. Pereira, and H.P. Urbach. Radially polarized light for detection and nanolocalization of dielectric particles on a planar substrate. *Physical review letters*, 114(10):103903, 2015.

[31] L. Scaccabarozzi, N.A. Lammers, R. Moors, and V. Banine. Cleaning and inspection of euv reticles : specifications and prospects. *ASML Netherlands*, 2013.

[32] M. Schnell, P.S. Carney, and R. Hillenbrand. Synthetic optical holography for rapid nanoimaging. *Nature communications*, 5(1):1–10, 2014.

[33] M. Schnell, M.J. Perez-Roldan, P.S. Carney, and R. Hillenbrand. Quantitative confocal phase imaging by synthetic optical holography. *Optics express*, 22(12):15267–15276, 2014.

[34] L. Schnitzler, Krisztian Neutsch, Falk Schellenberg, Martin R. Hofmann, and Nils C. Gerhardt. Confocal laser scanning holographic microscopy of buried structures. *Applied Optics*, 60(4):A8–A14, 2021.

[35] Toms. Grating stock photo. `https://www.freeimages.com/photo/grating-1200476`. Accessed: 2022-01-28.

[36] M. van de Kerkhof, T. van Empel, M. Lercel, C. Smeets, et al. Advanced particle contamination control in euv scanners. *Extreme Ultraviolet (EUV) Lithography X*, 10957:109570U, 2019.

[37] J. van der Donck, R. Snel, J. Stortelder, A. Abutan, S. Oostrom, S. van Reek, B. van der Zwan, and P. van der Walle. Particle detection on flat surfaces. *Extreme Ultraviolet (EUV) Lithography II*, 7969:79691S, 2011.

[38] J. Zhang, S. Dai, C Ma, T. Xi, J. Di, and J. Zhao. A review of common-path off-axis digital holography: towards high stable optical instrument manufacturing. *Light: Advanced Manufacturing*, 2(3):333–349, 2021.